Summer 2022

Acoustic Lens Design Using Machine Learning

Wei-Ching Wang
San Jose State University

ACOUSTIC LENS DESIGN USING MACHINE LEARNING

A Thesis

Presented to

The Faculty of the Department of Mechanical Engineering

San José State University

In Partial Fulfillment

of the Requirements for the Degree

Master of Science

by

Wei-Ching Wang

August 2022

The Designated Thesis Committee Approves the Thesis Titled

ACOUSTIC LENS DESIGN USING MACHINE LEARNING

by

Wei-Ching Wang

APPROVED FOR THE DEPARTMENT OF MECHANICAL ENGINEERING

SAN JOSÉ STATE UNIVERSITY

August 2022

Feruza Amirkulova, Ph.D.	Department of Mechanical Engineering
Ali Tohidi, Ph.D.	Department of Mechanical Engineering
Birsen Sirkeci, Ph.D.	Department of Mechanical Engineering

ABSTRACT

ACOUSTIC LENS DESIGN USING MACHINE LEARNING

by Wei-Ching Wang

This thesis aims to contribute to the development of a novel approach and efficient method for the inverse design of acoustic metamaterial lenses using machine learning, specifically, deep learning, generative modeling, and reinforcement learning. Acoustic lenses can focus incident plane waves at the focal point, enabling them to detect structures non-intrusively. These lenses can be utilized in biomedical engineering, medical devices, structural engineering, ultrasound imaging, health monitoring, etc.

Finding the global optimum through a traditional iterative optimization process for designing the acoustic lens is challenging. It may become infeasible due to high dimensional parameter space and the compute resources needed. Machine learning techniques have been shown promising for finding the global optimum. Generative modeling is a powerful technique enabling recent advancements in drug discoveries, organic molecule development, and photonics. We combined generative modeling with global optimization and an analytical form of gradients computed by means of multiple scattering theory. In addition, reinforcement learning can potentially outperform traditional optimization algorithms. Thus, in this thesis, the acoustic lens is modeled using two machine learning techniques, such as generative modeling, using 2D-Global Topology Optimization Networks (2D-GLOnets), and reinforcement learning using the Deep Deterministic Policy Gradient (DDPG) algorithm. Results from the aforementioned methods are compared with traditional optimization algorithms.

ACKNOWLEDGEMENTS

First and foremost, I would like to thank Dr. Feruza Amirkulova for serving as my thesis advisor. With her unwavering support and excellent guidance, I broadened my knowledge and skill sets in engineering. Her encouragement and inspiration have spurred me to have diverse and multidisciplinary perspectives in the physical sciences. I am appreciative of her great dedication to research and helping me to grow. She gave me opportunities to attend conferences domestically and internationally to present my research and learn from other scholars' research.

In addition, I would like to thank Dr. Birsen Sirkeci and Dr. Ali Tohidi for serving on my thesis committees and for their precious time participating in my thesis defense presentation and providing great ideas for my research. Their help means a lot to me.

Finally yet importantly, I would like to thank my parents for supporting me despite all the difficulties. Their great sacrifice and unconditional love have made a great impact in my life.

TABLE OF CONTENTS

LIST OF TABLES

LIST OF FIGURES

1. INTRODUCTION

Metamaterials [1], [2] are artificially engineered materials with properties not available in nature. Their capabilities surpass traditional materials and can manipulate sound, ultrasound, and vibrations as well as acoustic, elastodynamic, optical, electromagnetic, and mechanical waves. In this thesis, we consider sound scattering from planar configurations of multiple scatterers embedded in acoustic media, and develop effective machine learning techniques for the design of acoustic metamaterial lenses, by specifically employing deep learning (DL), generative modeling, and reinforcement learning (RL) techniques. The optimization methods such as gradient-based optimization algorithms, topology optimization, and genetic algorithms (GA) can search for optimal solutions in the acoustic design. However, due to the non-convexity and high non-linearity of the optimization problem, the realization of inverse design of broadband acoustic lens using traditional optimization algorithms may become computationally expensive and infeasible. Moreover, it is challenging to find a global optimum of the absolute pressure at the focal point operating at multiple frequencies using an iterative optimization process due to the form of the objective function, which involves the evaluation of the root mean square of the function evaluated at various wavenumbers [3], [4].

Recent research on nanophotonics [5], mechanics, and acoustics using RL and generative modeling has shown groundbreaking results [6]–[8]. The 2D-GLOnets [3] and Deep Deterministic Policy Gradient (DDPG) [6], have previously shown to be effective and promising method for finding globally optimal solutions [6], [7], [9]. Inspired by the tremendous success using RL [10]–[12] and generative modeling [13] to solve inverse design problems in nanophotonics and acoustics [6], we are going to model acoustic lens using RL

algorithms, such as DDPG, and to implement the generative model, such as the 2D-Global Topology Optimization Networks (2D-GLOnets) for acoustic lens design, leveraging the analytical gradient information provided to the model.

1.1. Literature Review

1.1.1. State-of-the-Art of Metamaterials

Metamaterials [1], [2] are artificially-engineered materials that can control and guide the flow of energy in a desired manner. Metamaterials have the exotic properties, i.e., wave steering [14], beam forming [15], negative Poisson ratio [16], negative mass density [17], [18], negative refraction [19], cloaking [20], [21], superfocusing [22], etc.

Metamaterials are used to design passive acoustic cloaks that can render an object "acoustically" invisible to the incident waves. Using the transformation acoustics or change-of-variables method to map the cloaked area to the point with diminishing scattering strength, the acoustic cloaking theory is developed first by Norris [20]. An acoustic cloak [20] is a device enclosing an object so that no matter from which directions the incident sound propagates, it passes around as if the object were not present. In 2010, Chen et al. [21] designed acoustic cloaks that surround or are located outside the object.

The interior cloaking involves steering waves around an object to conceal its presence [23]. The external cloaking is accomplished using complementary media and wave scattering cancellation [23]. In modern military technology, the "invisibility cloak" is particularly crucial in aerospace engineering applications, sonar and stealth technologies where objects that are cloaked are not detected by radar-like devices [23].

Another application of metamaterials is acoustic lenses made of metamaterial that can focus the incident plane waves at a certain focal point [3], [24]. Applications of acoustic lenses encompass biomedical imaging [25], ultrasonic transducers [26], and structural health monitoring [27]. Metamaterial lenses made from subwavelength Helmholtz resonators could focus ultrasound waves [28]. A focus with a width of 60.5 kHz and a half-wavelength is ascertained [28]. The experimental results are validated by the numerical simulation of the effective mass density and compressibility [28].

Besides, Semperlotti et al. [27] presented that acoustic lenses can be employed in structural health monitoring for structural damage detection. With the recent medical technology advancement, acoustic lenses can also be utilized to project ultrasonic beams at a desirable distance [29]. Improvements to the ultrasound-guided procedures can be made by implementing an acoustic metamaterial lens [26]. An acoustic lens was designed by Amirkulova et al. [3] using gradient-based optimization; the lens was comprised of a set of rigid cylinders or a set of elastic shells immersed in water.

Aside from acoustic lens, phononic crystal is another example of metamaterials. Unique properties, such as negative bulk modulus and negative mass density, can be achieved by manipulating a phononic crystal at the atomic level [30]. Zhou et al. [22] showed that acoustic superfocusing beyond the diffraction limit is possible with solid phononic crystal lenses [22]. It was found that it is more suitable for ultrasonic imaging applications to use solid lenses rather than fluid phononic lenses. As opposed to achieving superfocusing effects, Lu et al. [31] lately proposed using phononic lattices to suppress acoustic waves and vibration to mitigate sound pollution in the urban area.

Furthermore, metasurfaces are also of the most exciting applications of metamaterials. More recently, Li et al. [32] have demonstrated active self-tuning metasurfaces that have the ability to extend their bandwidth beyond that of passive electromagnetic wave absorbers. Possible applications include conformal antennas, leaky wave structures [32], etc. Patela et al. [33] designed biosensors using graphene metasurfaces. Graphene metasurfaces can be used to develop a leaky-wave structure and show high biosensing sensitivity. Therefore, its application will be impactful in biosensing technology. Patela et al. [34] also proposed a tunable broadband metasurface solar absorber at high and low frequencies. Future development of efficient solar cells can benefit from the solar design.

1.1.2. Traditional Optimization Methods

In 2004, Håkansson et al. [35] solved the inverse design of acoustic lenses made of cylindrical rigid scatterers for airborne sound focusing using genetic optimization algorithms and the multiple scattering theory (MST) [36]. In recent years, Reis et al. [37] proposed GA integrated with the asymptotic homogenization schemes for inverse design of lattice metamaterials. The linear elastic analysis design space has been explored regarding genetic representations of the optimization process. Sigmund [38] discussed how topology optimization could be applied to various fields, such as aerospace and automobile industries. Andkjær and Sigmund [39]–[41] modeled an acoustic cloak to obscure an aluminum cylinder from the airborne sound, utilizing finite element analysis (FEA) and gradient-based topology optimization. Topology optimization can be a valuable method in identifying the optimal topologies and shapes to maximize or minimize objective function and improve the design process [42]. It can be applicable in many fields, such as metamaterial [43], nanophotonics

[44], etc. Esfarjani et al. [43] provided a comprehensive review focusing on topology optimization of additive-manufactured metamaterial structures. Nguyen [45] employed topology optimization to design material microstructures with negative effective Poisson's ratio in unit cell geometries. A parameterized level set function is successfully applied to find the optimized design ready to get 3D-printed [45]. Besides, computation time can benefit from the feasibility of the reduced order modeling approach, but it requires more research in future work [45].

Amirkulova et al. [3], [46] developed a gradient-based optimization (GBO) approach to design acoustic cloaks and lenses. Amirkulova et al. [3], [47] derived analytical formulas for the gradients of absolute pressure at the focal point with respect to the scatterers' positions and supplied it to GBO algorithms for optimal optimization at multiple frequencies and angles of plane wave incidences.

Besides metamaterial design, Mattoso et al. [44] focused on nanophotonic structures that can concentrate energy. The governing equation is Maxwell's equations in the frequency domain. Specifically, the goal is to maximize the system's energy as a function of silicon dioxide and silicon distribution in a small region of the nanophotonic device utilizing the topological derivative method. Finally, experiments have been carried out to demonstrate hotspots with high energy density and validate the design.

1.1.3. Inverse Design Using Deep Learning

Applications of inverse design using DL encompass the design of nanophotonic devices [48], plasmonic waveguide systems [49], metasurface optical filters [50], etc. Campbell et al. [51] conducted a literature review on numerical optimization techniques for meta-devices.

The fully connected neural networks (FCNN) make it possible to learn the relation between geometric configuration and optical response. FCNN is particularly useful for the inverse design of nanophotonics. Peurifoy et al. [52] employed a FCNN to design an optical cloak and to expedite the design process to approximate the solution of the Maxwell equations. The FCNN is run reversely, with fixed output to the desired value, and lets the FCNN obtain good accuracy. Fan et al. [53] considered acoustic scattering utilizing a single scatterer as a 2D image-to-image regression problem using convolutional neural networks (CNN). Meng et al. [54] formulated the problem of inverse acoustic scattering using an FCNN to reconstruct the shape of an obstacle with far-field information. Han et al. [50]'s DL inverse model capable of generating a diverse range of device structures ensures speed and accuracy. One disadvantage of the model [50] is that certain conditions result in the disappearance of gradients. Li et al. [55] proposed tandem FCNN for inverse design of ultra-thin underwater acoustic metasurfaces at low frequency. This FCNN include a forward network that has been pretrained and a reverse network. A diffuse underwater acoustic metasurface was created [55] successfully using the designed metasurface elements. Ma et al. [56] implemented a deep-learning accelerated framework to design Magneto-mechanical metamaterials capable of satisfying specific target deformations with strain restriction. This DL model utilizes CNN to replace the used FEA software that is computationally expensive. A wide range of deformation tunability has been shown for magneto-mechanical metamaterials. However, it is time-consuming to prepare data set. Even though a larger amount of data is desired, they have limited capacity to collect it [56]. DL results [56] have been validated by using FEA software.

1.1.4. Generative Modeling in Inverse Design

Generative modeling searches for patterns in input data without supervision. Models are capable of generating their own data based on the original training dataset [57]. Generative models have the ability to learn a real distribution, and, therefore, are helpful in inverse design [57]. With the nature of generative modeling, automated design synthesis can revolutionize engineering design in the modern era [57]. Particularly, generative modeling can be applied to engineering-related problems to enable automated design synthesis. Applications of generative modeling include acoustics [58], material science [59], and imitation learning [60]. Therefore, generative modeling has been applied to solve various inverse design problems [59] where generating the data can be expensive or when data is not available. Inverse materials design will be aided by data-driven generative models with high-performance computations and material databases [59]. Studies have demonstrated that the performance of the generative model is contingent on training dataset quality and size [59]. Despite the possibility of high-speed fundamental calculations used to create material portfolios, it takes considerable time when structures get complex [59].

Generative Adversarial Network (GAN) [61], GLOnets [13] and Variational Autoencoder (VAE) [62] are three commonly used network architectures for material design which will be discussed next.

1.1.5. Generative Adversarial Networks (GANs)

Lately, GANs [13], [63], [64] have been triumphant and viable in recent years. Boget [65] presented promising results using GANs for adversarial non-linear regression, provides excellent estimation and approximates the probability density function. The conditional GAN

(cGANs) [63] is capable of performing multi-modal learning. The Wasserstein GAN (WGAN) [64] has been proven to enhance the stability of learning and avoid mode collapse. Developments of the inverse design of molecular components [66], metasurfaces [13], and optical cloaks [67] benefited from using deep generative models. It has been exhibited that using GANs, a global optimizer for dielectric metasurfaces, can be built in the field of electromagnetism [68]. In recent work, Gurbuz et al. [69] used conditional GANs annexed with finite element simulation carried out in COMSOL, a multiphysics simulation software, to create acoustic metamaterials for broadband sound insulation. Lai et al. [8] implemented conditional WGANs for total scattering cross section (TSCS) suppression. This model [8] integrates the WGANs with CNN and CordConv layer [70]. Due to the similar nature of electromagnetic and acoustic waves [9], [68], the similar idea of optimizing the electromagnetic waves will be utilized for our cloak design.

1.1.6. GLOnets: Combining Global Optimization with Generative Modeling

As an alternative to GAN, Jiang and Fan [13], [71] proposed a generative model for a design of 1D metagratings. Fan's group [13], [71], [72] proposed a global optimization technique, a generative modeling combined with gradient-based optimization. Unlike the traditional optimization scheme, the proposed 1D-GLONets consider a population of optimal devices simultaneously. The 1D-GLONets optimizes the deflection efficiency as a function of wavelength and outgoing angle. Chen et al. [73] further proposed reparameterization that applies to 1D-GLOnets to impose geometric constraints to constrain the devices.

Motivated by the works of Fan's group [13], [71], [73], Zhuo and Amirkulova [7], [9] generalized this idea to solve 2 dimensional (2D) constrained optimization problems and

implemented a 2D-GLOnets generative model for broadband acoustic cloak design where the gradient information [46] was used to update the weights of the generator. They successfully showed exciting results that outperformed conventional optimization solver *fmincon*. It has been shown [7] that the 2D-GLOnets outperformed traditional optimization algorithms, which motivates us to apply the 2D-GLOnets model developed by Zhuo and Amirkulova [9] to the acoustic lens design problem.

1.1.7. Variational Autoencoders

Variational Autoencoders (VAE) are a deep generative model that consists of an autoencoder that can reduce dimensions and extract features [59]. In molecular informatics, Blaschke et al. [74] investigated the effectiveness of generative autoencoders in mapping molecule structures into continuous latent spaces. Novel chemical structures are generated using inverse quantitative structure-activity relationship and generative adversarial autoencoders [74]. Utilizing a probability distribution as a constraint on the encoder networks, VAE allow for better generalization [75]. A scalable integrated architecture for the data-driven metamaterial design at multiple scales is presented, employing the continuous and structured latent space of the VAE model [76]. Wang et al. [76] integrated VAE with a regressor for mechanical engineering properties, such as stiffness matrix, etc. The generative neural networks model extracts characteristics [76]. Mechanical properties can be tuned, and candidate structures are generated following the extracted features. Results show the latent space vector arithmetic can be employed to map microstructure topology and mechanical properties [76]. One huge advantage of the model is that it can consider metamaterial families and multiscale metamaterial systems design [76]. Nevertheless, the current model

only depends on the homogenization theory that considers the linear elasticity of materials. In addition, Ahmed et al. [58] introduced DL techniques that have a network similar to autoencoders and VAE for the inverse design of an acoustic cloak. The autoencoder-like [58] networks, consisting of an inverse network followed by a pre-trained forward network, implement the core-shell acoustic cloak with multiple layer thicknesses and spectral response. The forward network is responsible for the design parameters and spectral response relationships. The inverse network is accountable for the relationship between the spectral response predicted by the pre-trained forward network and the design parameters [58]. One drawback of the model is that growing the number of layers raises the complexity, which significantly increases the training time [58].

Tran et al. [77], [78] proposed conditioning can be performed using two methods: supervised VAE (SVAE) and conditional VAE (CVAE) for acoustic cloak design with minimal TSCS. FCNN serves as the forward design. In inverse design, combining VAEs, supervised and unsupervised learning, and the Gaussian process predicts optimal scatterer arrangements for a minimal TSCS [79]. The SVAE model is constructed with a neural network regressor that takes the encoded latent variables z as input and predicts TSCS based on the latent variables. A concatenation of latent variables z with TSCS and CVAE. The latent variables are conditioned to reflect TSCS; therefore, the neural networks model is allowed to encode the physics of the problem. Intriguingly, Ahmed et al. [80] utilized a variational inference approach in an encoder-decoder architecture in which the decoder possesses a pre-trained generator and a forward model [80]. Results showed great accuracy for phaseless acoustic scattering. One of the model's advantages is that complex calculations

are not required. The method could be further extended to automatic recognition of underwater objects [80].

1.1.8. Deep Reinforcement Learning in Inverse Design and Optimization

More recently, deep reinforcement learning (RL) [5] is an essential part of the field of machine learning. It enables automating tasks performed by agents [81]. Deep RL applications include adaptive control, autonomous driving, planning in chess, job-shop scheduling, robotics, etc [82]. More recently, model-free deep reinforcement learning [5] has been applied in inverse design of molecule structures [83]–[89], photonic devices [90]–[92], and of acoustic metamaterials [6].

A properly trained networks can lead to high performance beyond the parameters provided in the training dataset. So et al. [93] examined the state-of-the-art work done on inverse designs of nanophotonics using RL [5] algorithms. Lengeling et al. [94] elaborated on the latest R&D in reverse molecular design, reviewed the methods to obtain reverse designs, and focused on customized materials from the starting point of specific required functions.

In RL, an agent intends to make the best decision in accordance with the given reward at each step [90]. It has been proven that the RL algorithms, such as AlphaZero and AlphaGo Zero, are capable of mastering chess, shogi, and Go through Self-Play. The AlphaZero algorithm, utilizing Monte Carlo Tree Search, is able to teach itself to play chess, shogi, and Go [95]. Sajedian et al. [90] utilized a Double Deep Q networks (DDQN) to increase the efficiency of the metasurface's hologram structure. Thanks to implementing neural networks, DDQN not only optimizes but also learns from the problem. The algorithms search for the

parameter space to find the highest reward in the least time possible. The input for DDQN is the initial structure of the design. The DDQN model structure is where the simulating environment serves as feedback. The structure state consists of geometrical properties and types of the structure material. The agent is awarded or penalized by the reward system based on the action selected.

In addition to DDQN using a discrete action space, the Deep Deterministic Policy Gradient (DDPG) introduces the idea of the use of a replay buffer and a separate target network [96], [97]. DDPG uses an actor-critic method and continuous action space. The actor in DDPG maps the state to a deterministic action [97]. It significantly improves the stability of training process [97]. Shah et al. [6] employed DDQN and DDPG algorithms to search for design parameters of scatterers that reduced the root mean square of the TSCS and to implement acoustic cloak. The gradient of the pressure amplitude function was utilized to accelerate calculation speeds. It was ascertained that the performance of DDPG generally performed better than that of DDQN [6].

In addition, the DDPG has various applications, such as control engineering [98], molecular generation [99], optimal drug dosing for patients [100], etc. The DDPG can be applied to docking an autonomous underwater vehicle (AUV) to an underwater platform. The DDPG model allows the AUV to attain performance comparable to optimal control [98]. This DDPG model [98] shortens the docking time. However, its bang-bang control behavior is hard to achieve due to physical limits in reality. Therefore, a change in the loss function might be required to improve the model [98].

In oncology, several factors, including the stage of the tumor, the patient's weight, and the white blood cell count, determine the optimal treatment schedule and drug dose [100]. Therefore, chemotherapy treatment must be properly scheduled and personalized to lower the patient's survival rate. Optimal scheduling for patients can benefit from DDPG and DDQN [100]. Even though the RL algorithms, such as DDPG and DDQN, are not as optimal as the traditional optimization techniques, it has been shown that the RL algorithms have the potential to outperform conventional optimization algorithms. Additionally, DDPG offers better performance and learns more rapidly thanks to continuous action space [100].

The structure of 3D chemical molecules can be predicted using conventional algorithms, such as stochastic iterative processes. Traditional algorithms are generally computationally expensive. Kim et al. [99] have demonstrated that the water structure predicted by DDPG is the same as the density functional theory calculation. However, one of the disadvantages of the DDPG model is slow convergence; therefore, the reward function might need to be modified [99].

1.2. Research Outline

The thesis consists of 6 chapters. Chapter 2 presents methodologies and acoustics preliminaries. The problem formulation and machine learning framework for acoustic lens design will be described. Chapter 3 introduces the 2D-GLOnets model architecture and discusses the 2D-GLOnets generative model results for acoustic lens design. Chapter 4 introduces fundamentals of RL and elaborates on RL results for broadband acoustic lens design. Chapter 5 summarizes the findings of the thesis. Chapter 6 describes future work.

2. METHODOLOGIES AND ACOUSTICS PRELIMINARIES

2.1. Problem Formulation

We consider multiple scattering in the context of the acoustic time-harmonic wave equation in two dimensions. The governing equation for the acoustic pressure $p(\mathbf{x})$, $\mathbf{x} \in \mathcal{R}^2$, is the Helmholtz equation [3]:

$$\nabla^2 p + k^2 p = q, \tag{2.1}$$

where $k = \omega/c$ is the wavenumber, c is the acoustic speed, ω is the frequency, and q represents the sources. In problems considered in this thesis, we do not take into account sources, i.e., $q = 0$, but consider a normal plane wave incidence to realize the Luneburg lens behavior. Note that the acoustic Luneburg lens can focus the plane incident wave on the other side of the lens at the focal point.

The particle velocity in the fluid $\mathbf{v}$ is related to the pressure by the momentum equation given by [101]:

$$-i\omega\rho f v = -\nabla p, \tag{2.2}$$

where p_f is the mass density of fluid. c and ρ_f are constants.

The total acoustic pressure field $p(\mathbf{x})$ is defined as the sum of incident p_{inc} and scattered p_{sc} pressure fields:

$$p = p_{inc} + p_{sc}. \tag{2.3}$$

Time harmonic dependence $e^{-i\omega t}$ is assumed but omitted in the following.

The incident field is a plane wave interacting with a given configuration of *M* separate scatterers. For simplicity, we consider circularly cylindrical scatterers, such as rigid cylinders shown in Fig 1.

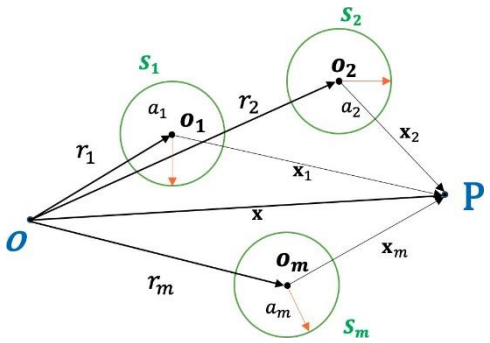

Fig. 1: An arbitrary planar configuration of *M* rigid cylinders S_m with radius a_m, $m = 1, M$ and position vector $\mathbf{r}_m$. The vector $\mathbf{x}$ describes the position of arbitrary point *P* with respect to origin *O*.

For a single scattering problem, the coefficients of scattered pressure B_n are related to incident field coefficients A_n in T-matrix form and comply with the continuity of displacement and pressure at the interface $r = a$ and are as follows [102]:

$$B_n = T_{nn}A_n \tag{2.4}$$

where T_{nn} are components of transition matrix **T** [102]. For rigid cylinders, the transition matrix components are of the form:

$$T_{nn} = -\frac{J_n'(ka)}{H_n^{(1)'}(ka)} \tag{2.5}$$

where *ka* is a normalized wavenumber, $J_n(x)$ is the Bessel function of the first kind of order *n*, $H_n^{(1)}(x)$ is the Hankel function of the first kind of order *n*.

Following [3], our goal is to maximize the acoustic pressure at the focal point by rearranging the positions of scatterers denoted by the set of vectors $\{\mathbf{r}_m\}$ as shown in Fig. 1. The focal point is at $\mathbf{x}_f$; it is fixed and pre-defined as depicted in Fig. 2.

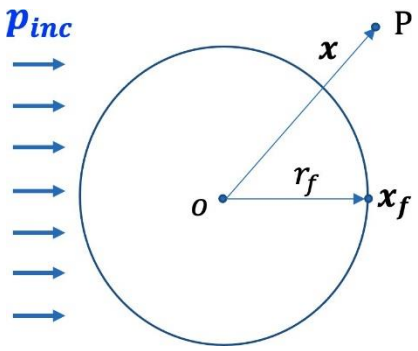

Fig. 2: Near-field of the focal point $\mathbf{x}_f$. The plane incident wave of unit amplitude is denoted by p_{inc}. The $\mathbf{x}$ is the position of arbitrary point P. The r_f is the magnitude of vector $\mathbf{x}_f$.

In accordance with Amirkulova et al. [3], we define p_f or equivalently p_f ($\{\mathbf{r}_m\}$) to be the total acoustic pressure at the focal point for a given set of the position vectors $\{\mathbf{r}_m\}$:

$$p_f(\{\mathbf{r}_m\}) = p(\mathbf{x}_f). \tag{2.6}$$

The absolute value is $|p| = (pp^*)^{1/2}$, and * denotes the complex conjugate.

2.2. Position Dependent Acoustic Pressure Field at the Focal Point

The total field $p(\mathbf{x})$ is defined by Equation 2.3 as the sum of incident p_{inc} and scattered p_{sc} pressure fields, $\mathbf{x}$ is a position vector of point P with respect to origin O. The incident wave is the plane wave of unit amplitude in direction ψ and the plane incident pressure at fixed focal point P_f is:

$$p_{inc}(\mathbf{x}_f) = e^{ike\psi\cdot\mathbf{x}_f}. \tag{2.7}$$

The scattered field in the neighborhood of cylinder S_m is given by [3]

$$p_{sc}(\mathbf{x}) = \sum_{m=1}^{M} \sum_{n=-\infty}^{\infty} B_n^{(m)} V_n^{+}(\mathbf{x}_m) \tag{2.8}$$

where $\mathbf{x}_m$ is a position vector of point P with respect to the cylinder center at O_m:

$$\mathbf{x}_m = \mathbf{x} - \mathbf{r}_m, \tag{2.9}$$

and the function $V^{\pm}(\mathbf{x})_n$ is defined as

$$V_n^{\pm}(\mathbf{x}) = H_n^{(1)}(k|\mathbf{x}|)e^{\pm i n \arg \mathbf{x}}, \tag{2.10}$$

where $H_n^{(1)}$ is the Hankel function of the first kind of order n.

Introducing Equation 2.7 and Equation 2.8 into Equation 2.3 and evaluating it at the focal point p_f defines the total pressure at the fixed focal point [3]:

$$p_f = e^{ik\mathbf{e}_\psi \cdot \mathbf{x}_f} + \sum_{m=1}^{M} \sum_{n=-\infty}^{\infty} B_n^{(m)} V_n^{+}(\mathbf{x}_f - \mathbf{r}_m). \tag{2.11}$$

Putting this formula into practice, it is mandatory that the infinite sum in Equation 2.11 be truncated, and that this equation be vectorized. To carry this out, let N be the truncation value of the infinite sum in Equation 2.11 chosen; therefore, the sum converges. Practically, the value of N depends on frequency. We select the value as: $N = 2ka$. We define $\mathbf{b}$, $\mathbf{v} \in C^{M\times(2N+1)}$. The components of the scattering coefficient vector $\mathbf{b} = \{ B_n^{(j)}\}$, $j \in (1,M)$, $n \in (-N, N)$, and $B_n^{(j)} = \{B_n(\mathbf{r}_j)\}$, and written in the column vector form [3]:

$$\mathbf{b} = \begin{pmatrix} \mathbf{b}^{(1)} \\ \mathbf{b}^{(2)} \\ \vdots \\ \mathbf{b}^{(M)} \end{pmatrix}, \quad \mathbf{b}^{(j)} = \begin{pmatrix} B_{-N}^{(j)} \\ B_{-N+1}^{(j)} \\ \vdots \\ B_{N}^{(j)} \end{pmatrix}. \tag{2.12}$$

The elements of the dual vector $\mathbf{v} = \{V^{(j)}\}_n = \{V_n(\mathbf{r}_j)\}$ were defined into the form [3]:

$$V_n^{(m)} = V_n^{+}(\mathbf{r}_{fm}), \tag{2.13}$$

where

$$\mathbf{r}_{fm} = \mathbf{x}_f - \mathbf{r}_m,$$

is the position of focal point with respect to local coordinate at O_m and $\mathbf{r}_m$ is the position of scatterer with respect to origin at O. Then the total pressure field at the focal point can be written in vector form as [3]:

$$p_f = e^{ik_e \psi \cdot \mathbf{x}} f + \mathbf{v}^T \mathbf{b}. \tag{2.14}$$

2.2.1. Absolute Pressure Amplitude and its Gradients with Respect to Scatterers' Positions

To perform broadband optimization, we chose our objective function as root mean square (RMS) of a set of absolute pressure at the focal point $|p_f|$ evaluated over some range of normalized wavenumbers $k_i a$ (i = 1, 2, ..., N_k), i.e., $|p_f(\{\mathbf{r}_m\})|^{RMS}$ [3]:

$$|p_f(\{\mathbf{r}_m\})|^{RMS} = \left(\frac{1}{N_k}[|p_f(k_1 a, \{\mathbf{r}_m\})|^2 + |p_f(k_2 a, \{\mathbf{r}_m\})|^2 + \ldots + |p_f(k_{N_k} a, \{\mathbf{r}_m\})|^2]\right)^{1/2}. \tag{2.15}$$

The real valued vector $\mathbf{q}_j$ defined as gradient of the absolute value of total pressure field $|p_f(\{\mathbf{r}_m\})|$ with respect to positions $\mathbf{r}_j$ was evaluated in [3] as:

$$\mathbf{q}_j = \frac{\partial |p_f|}{\partial \mathbf{r}_j} = \frac{1}{2|p_f|}\frac{\partial |p_f|^2}{\partial \mathbf{r}_j} = \frac{1}{2|p_f|}(p_f^* \mathbf{p}_j + p_f \mathbf{p}_j^*), \tag{2.16}$$

where * indicates the complex conjugate, $|p_f|$ is defined by Equation 2.14, and the relevant complex valued gradient vectors are:

$$\mathbf{p}_j = \frac{\partial p_f}{\partial \mathbf{r}_j}. \tag{2.17}$$

The broadband gradient vectors were defined with respect to positions $\mathbf{r}_j$:

$$\mathbf{q}_j^{RMS} = \frac{\partial |p_f(\{\mathbf{r}_m\})|^{RMS}}{\partial \mathbf{r}_j}, \quad j = 1, 2, \ldots M, \tag{2.18}$$

which was found in terms of the individual single frequency gradients as [3]:

$$\mathbf{q}_j^{RMS} = \frac{1}{|p_f|^{RMS}}\frac{1}{N_k}\left(|p_f(k_1 a)|\mathbf{q}_j(k_1 a) + |p_f(k_2 a)|\mathbf{q}_j(k_2 a) + \ldots + |p_f(k_{N_k} a)|\mathbf{q}_j(k_{N_k} a)\right), \tag{2.19}$$

where $|p_f|^{RMS}$ is defined by Equation 2.15 and $\mathbf{q}_j(k_i a)$ are defined by Equation 2.16 and evaluated at normalized wavenumbers $k_i a$ (i = 1, 2, ..., N_k).

2.3. Neural Networks Fundamentals

In this thesis, we combine DL with generative modeling and reinforcement learning. Therefore, it is imperative to provide the basics of neural networks architecture. The FCNN, as illustrated Fig. 3 are comprised of neurons, an input layers, an output layers, and one or multiple hidden layers in between [103]. Neurons are interconnected in the adjacent hidden

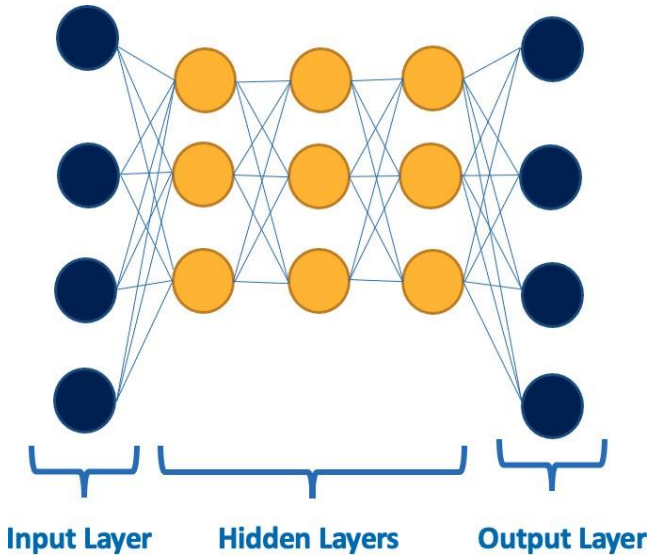

Fig. 3: Simple neural networks, FCNN, showing the input layer, output later, and hidden layers.

layers. The layer between the output and input layer is called the hidden layer [104]. The hidden layer helps determine the importance of the inputs with respect to the outputs.

The weights scalar w_i and biases scalar b are the most essential part of the FCNN. Referring to Fig. 4, using weights w_i, the FCNN can make connections between neurons stronger or weaker. By adjusting the weight w_i of inputs, the networks can adjust the strength of the connections between neurons in the next layer. Adjustments can be made within neurons using bias b. Biases b can increase or decrease a neuron's output, depending on the signs of a bias b. The sum of the inputs multiplied by the corresponding weights plus the bias b is passed to the activation function. An activation function determines whether a neuron should be activated, deciding whether the neuron's input to the networks is important. There are some popular activation functions, such as rectified linear activation (*ReLU*) [105], hyperbolic tangent (*Tanh*) [105], and others [103].

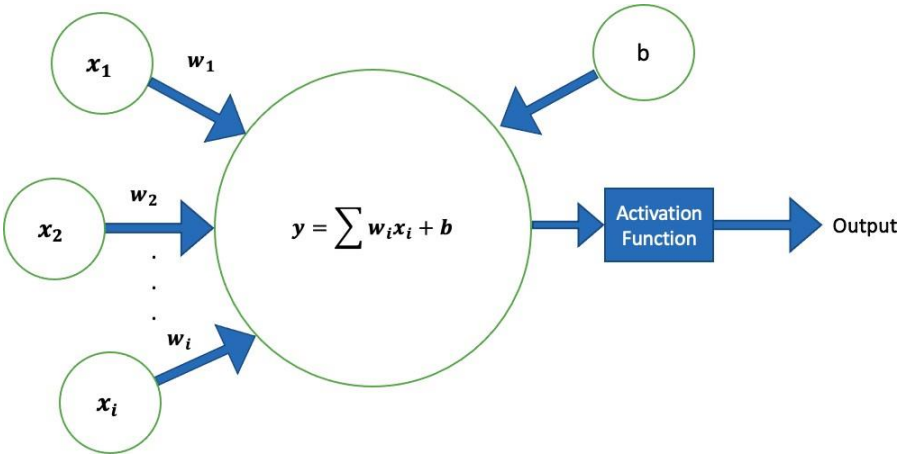

Fig. 4: FCNN weights x_i and biases b: A simple mathematical operation for sum of weighted input from the node.

During the training, weights w_i in FCNN are initially random numbers. Next, the FCNN takes one input, predicts, and assesses the prediction's accuracy. Backpropagation is a commonly used technique to calculate derivatives efficiently. The FCNN propagates errors from the output layer to the input layer by calculating the loss function with respect to weights w_i. By adjusting the weights w_i, the FCNN predicts more accurately given the same input data point at a later time. Making a prediction renders the FCNN more accurate every time [104]. Currently, we can utilize various useful tools, including Keras, TensorFlow, PyTorch, Julia, Matlab, etc., to implement neural networks architectures.

2.4. Predicative Model Using DL

We utilized Matlab code employing MST to compute the total scattering cross section (TSCS) given various random planar configuration of cylinders. We generate 60, 000 random planar configuration of cylinders. The number of the cylinders M considered varied from 2 to 20 with an increment of 2. We evaluate TSCS for each configuration at various rages of normalized wavenumbers $ka \in [0.35, 0.45]$ and $ka \in [1.35,1.45]$. Next, we generate 200 by

200 pixel size binary images of planar configurations of cylinders indicated as input in Fig. 5. The input consists of image matrices with 200 by 200 in dimension. The output is the TSCS evaluated at 11 values of wavenumber *ka* for each configuration. The data were split into training and test data in a 7:3 ratio.

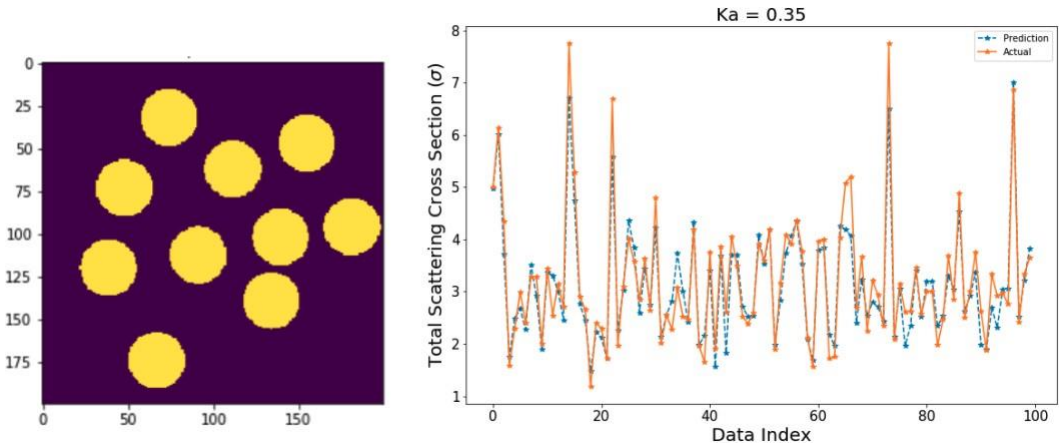

Fig. 5: An example of image of configuration of $M = 10$ scatterers (left). The TSCS predictions at the wavenumber $ka = 0.35$ for $M = 10$ for 100 randomly chosen data (right).

It has been shown that the acoustic TSCS can be approximated at 11 discrete values of frequency using FCNN and CNN [106]. Specifically, the TSCS by a plane configuration of cylinders is approximated over a range of wavenumbers using trained FCNN. The forward design only allowed for approximating the TSCS. The input of neural networks is the positions of the cylinders, and the output is the TSCS evaluated at discrete values of wavenumber. Neural networks are trained to approximate the TSCS function using the backpropagation algorithm [106], [107]. The TSCS is approximated over a range of wavenumbers to develop the efficient design of broadband acoustic cloaks. Combining these FCNN and CNN models with generalized models, the inverse design was solved by using cWGAN [4] and cVAE [77].

Fig. 6 illustrates a CNN architecture used for TSCS prediction. The CNN consists of an input picture, convolutional layer, polling layer, and an FCNN. The input of CNN is a binary image matrix showing the configuration of scatterers. The output is the TSCS prediction. Essentially, the TSCS by a plane configuration of cylinders was approximated over a range of wavenumbers using trained FCNN and CNN. Fig. 5 shows the TSCS prediction results with 10 cylinders using CNN at the wavenumber $ka = 0.35$. The prediction by CNN shows high accuracy. In general, the prediction at the low frequencies, i.e., $ka \in [0.35, 0.45]$, performs better than the prediction at the high frequencies, i.e., $ka \in [1.35, 1.45]$ due to the non-linearity of the physics at high frequencies.

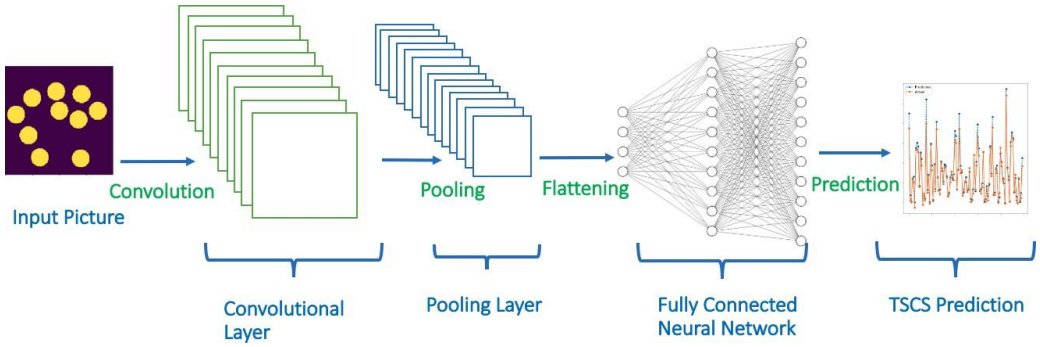

Fig. 6: CNN structure used for TSCS prediction

2.5. Machine Leaning Framework for Acoustic Lens Design

Amirkulova et al. [3], [46] used metamaterial design using gradient-based optimization algorithms. In this project, we combine funding of [3] and [46] and integrate the inverse design with reinforcement learning [6] and generative modeling [9]. A novel method [108]–[110] will be provided to simulate multiple acoustic scattering by configuring cylinders and solving inverse design problems using DL. This research aims to examine and evaluate the performance of generative networks and RL searching for optimized configuration of

scatterers over a range of parameters to produce desired functionality such as focusing and localization effects. We will train the agents in RL models to discover the optimal policy that locates the optimized configurations. In this thesis, we adopt the idea presented by Shah et al. [6] for acoustic cloak design to design broadband acoustic lenses. The position and radius of the scatterers are the design parameters. RL algorithms, such as DDPG, will be utilized to maximize absolute pressure amplitude at the focal point for acoustic lens design. The agent receives a positive reward proportional to the root mean square pressure amplitude across a range of frequencies at the focal point. Ultimately, the designs with the maximum absolute pressure amplitude at the focal point will be ascertained. The DDPG architecture developed by Shah et al. [6] is adapted to our acoustic lens design.

In addition, the 2D-GLOnets have been proven [9] to give good results for acoustic cloak design. The model maximizes the probability of generating globally optimized devices within the design space. We adapted the 2D-GLOnets model developed by Zhuo et al. [9] and modified and tune it for the inverse design of broadband acoustic lenses by combining the generative networks with gradient-based optimization.

2.5.1. Geometric Constraints

The geometric constraints are imposed to control the positions of the rigid cylinders at each iteration as shown in Fig. 7. It is essential that the following constraints are satisfied:

1. Bound Constraints: The center of the rigid cylinders x_j, y_j needs to be located inside the $x \in [-10, 10]m$ and $y \in [-10, 10]m$.

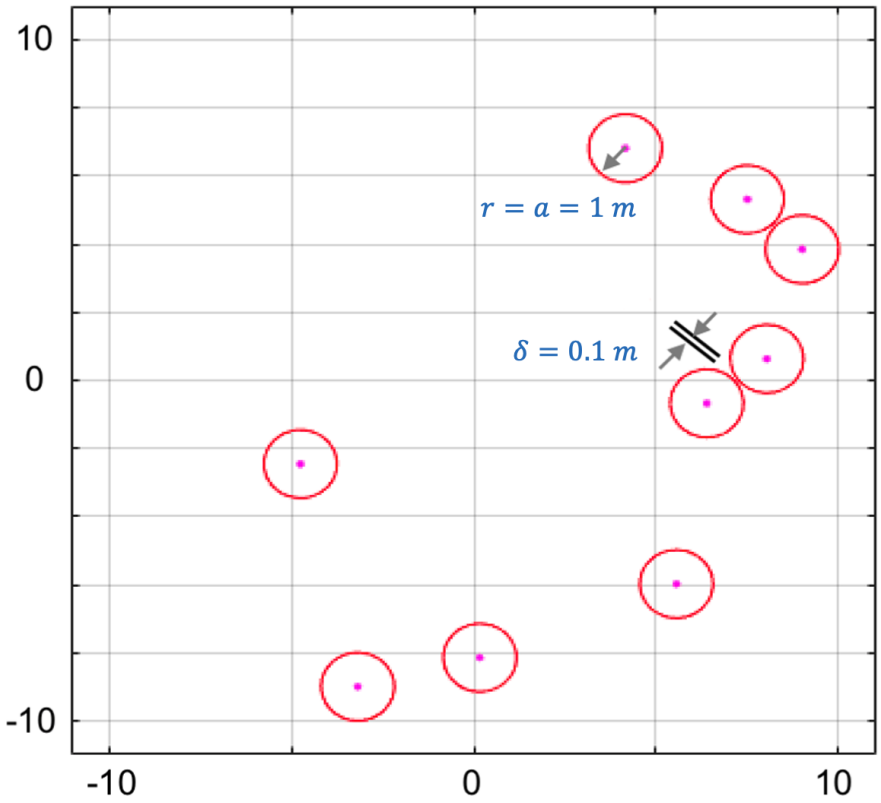

Fig. 7: The illustration of 2D geometric constraints with $\delta = 0.1m$ and $r = a = 1m$.

2. Nonlinear Constraints: Overlapping of rigid cylinders is not allowed. The distance between the position vector of two different rigid cylinders $\mathbf{r}_m$ and $\mathbf{r}_n$ must be greater than the diameter $2r$ of the rigid cylinders with a minimum allowed distance δ [3] given by:

$$|\mathbf{r}_m - \mathbf{r}_n| > 2r + \delta \tag{2.20}$$

where the minimal distance δ is chosen as 0.1 and $r = a = 1m$ in simulations.

3. 2D-GLONETS GENERATIVE MODEL FOR ACOUSTIC LENS DESIGN

3.1. Architecture

The 2D-GLOnets generative model has previously shown to be effective in acoustic cloak design [7], [9]. This method can find globally optimized solutions while imposing geometric constraints to control the scatterers. Therefore, the 2D-GLOnets are used to design acoustic lenses.

Fig. 8 shows a machine learning framework, the 2D-GLOnets, that can be utilized for the inverse design of the acoustic lens. In this framework, the Gaussian noise of size of 1 by 128 is an input passed into the generator. The generator serves as a device to generate unconstrained configurations of the scatterers. The generator is comprised of the architecture of the FCNN of 8 layers. The input is concatenated in the generator with a size of 1 by $U \times M = 128$, where U is the batch size, and M is the number of the scatterers. An activation function of *LeakyReLU* is employed from the first layer to the seventh layer, and an activation function of *tanh* is used in the last layer. All 2D-GLOnets hyperparameters are tabulated in Table 1. The batch size specified for each M at the 2 frequency ranges is tabulated in Table 2.

Amirkulova et al. [47] utilized the principle of reciprocity and gradient-based optimization to design broadband acoustic lenses; this method uses an analytical form of gradients. An analytical form of the pressure gradient at the focal point with respect to positions of a set of cylindrical scatterers was evaluated [3] to model the acoustic lenses for underwater applications [3], [47]. Since the gradients are evaluated analytically, they can be provided to GBO algorithms to enhance modeling, to improve the accuracy of results, and to

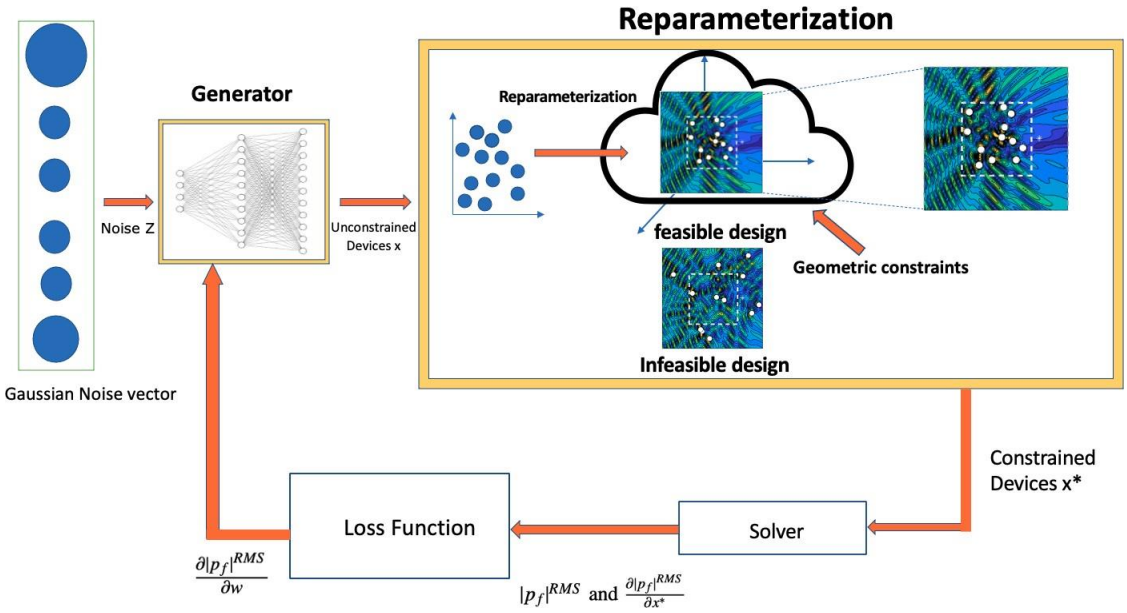

Fig. 8: 2D-GLOnets architecture including Gaussian noise vector, generator, reparametrization, pressure amplitude, loss function, and multiple scattering solver that evaluates RMS of pressure amplitude at the focal point, i.e., $|p_f|^{RMS}$ and its gradients. Details about each component will be elaborated in Section 2.3 and Section 2.4.

reduce computation time [3], [46], [47]. In this work, we will utilize the analytical form of pressure gradient at the focal point to compute and update weights of the generator.

3.2. Reparametrization

In the original 1D-GLOnets model [71], the problem is formulated as a design of 1D metagratings where the position of metagrating is fixed which does not require any geometrical constraints, allowing the model to change other parameters, i.e., outgoing angle and wavelength. In this model [71], the input of the generative architecture is the wavelength, outgoing angle, and noise vector, and the output of the generator is a binary image of a 1D metagrating structure generated for a variety of parameter settings.

Table 1: 2D-GLOnets Hyperparameter Table

Hyperparameters	**Values or descriptions**
Batch size U	M-dependent
Tunable hyperparameter σ	M-dependent
Constrained device x^*	Variable
Gradients of unconstrained device with respect to constrained device $n^{(\gamma)}$	Variable
Gradient q for a batch of Γ devices $\mathbf{q}_i^{RMS}$	Variable
Optimizer	*ADAM*
Radius of the scatterers r	1.0
Learning rate Ir	0.001
Noise dimension vector size	(1, 128)
Noise scale	1.0
Number of generator hidden layers	8
Generator hidden layers' sizes	64, 128, 256, 256, 128, 64
Number of generator's input layer	32
Number of generator's output layer	32
Activation function for generator's hidden layers	*LeakyReLU*
Activation function for generator's last layer	*tanh*

Table 2: Batch Size with Varying M at 2 Wavenumber Ranges Table

M	4	5	6	7	8	9	10	11	12
ka ∈ [0.35, 0.45]	100	100	100	3	10	10	15	2	2
ka ∈ [1.35, 1.45]	80	80	80	6	10	15	2	2	2

Zhuo and Amirkulova [7], [9] developed 2D-GLOnets for broadband acoustic cloak design by generalizing the 1D-GLOnets [71] and by introducing the reparametrization step to this model. The implementation of these reparametrization techniques allowed the solution of

a constrained optimization problem that generated images of configurations should avoid overlapping of scatterers. In this work, we adopt 2D-GLOnets [7], [9] and use this reparameterization scheme for acoustic lens design. The reparameterization converts the unconstrained device X into the constrained device X^*. The purpose of the reparametrization is to avoid overlapping the cylinders and to confine the cylinders to a constrained region as described in Section 1.5.1. The methodology is adapted from the idea of training multiple agents to perform a collaborative task in MATLAB [111]. Newton's second law is applied to the cylinders with a pre-assigned mass. A force pulls the cylinders apart when they overlap or when a cylinder touches the wall. The loop updates itself unless the geometric constraints are fully satisfied. After the reparameterization, a constrained device x^* is passed to the MATLAB solver that computes the RMS absolute pressure amplitude at the focal point $|p_f(\{\mathbf{r}_m\})|^{RMS}$ and the gradients with respect to position vectors, which are further passed into a loss function that generates a partial derivative of absolute pressure with respect to the weights, which are updated during each iteration.

3.3. Loss Function

To formulate the loss function for the 2D-GLOnets, we follow Zhuo and Amirkulova [9] and adapt the idea from Chen et al. [73] who defined the loss function in the form:

$$L = -\frac{1}{K}\sum_{k=1}^{K}(1/\sigma)exp\frac{Eff^{(k)}}{\sigma}\boldsymbol{\epsilon}^{(k)}\cdot\mathbf{g}_e^{(k)}, \tag{3.1}$$

where $Eff^{(k)}$ are the efficiencies, $\mathbf{g_e^{(k)}}$ are the efficiency gradient vectors, σ is a hyperparameter, $\boldsymbol{\epsilon}^{(k)}$ are globally optimized devices, and K is the batch size. The loss function defined by Equation 3.1 minimizes the probability that the neural networks will provide the

optimal latent vector that correlates to the globally optimized device. It is previously shown that the loss function of the GLOnets can be applied to inverse design of nanophotonic devices [73].

Similar to the structure of the loss function proposed by Chen et al. [73], Zhuo and Amirkulova [9] proposed a loss function for 2D-GLOnets that minimizes the TSCS function:

$$L(x, g_\epsilon, \sigma_{RMS}) = \frac{1}{K}\sum_{k=1}^{K}\frac{1}{\beta}\exp\left[\frac{\sigma_{RMS}(x^{(k)^*}) - \sigma_{RMS\,min}}{\beta}\right]\cdot\frac{\partial x^{(k)^*}}{\partial x^{(k)}}\cdot\frac{\partial \sigma_{RMS}}{\partial x^{(k)^*}}, \tag{3.2}$$

where β is a hyperparameter, K is the batch size, $\frac{\partial x^{(k)^*}}{\partial x^{(k)}}$ are the gradients of the unconstrained devices with respect to the constrained device, $\frac{\partial \sigma_{RMS}}{\partial x^{(k)^*}}$ is a gradient $\mathbf{q}$ for a batch of K devices, and $\sigma_{RMS\min}$ is the minimum RMS TSCS at the given iteration. For the acoustic lens design, our goal is to maximize the RMS of absolute pressure amplitude at the focal point. The ideas from Zhuo and Amirkulova [9] and Chen et al. [73] were considered to construct the loss function of the training of the acoustic lens model defined as:

$$L = -\frac{1}{\gamma}\sum_{\gamma=1}^{\Gamma}(1/\sigma)exp\frac{|p_f^{(rms)}(x^\gamma)|}{\sigma}\cdot\mathbf{n}^{(\gamma)}\cdot\mathbf{q}_\mathbf{j}^{\mathbf{RMS}}, \tag{3.3}$$

where γ is the number of unconstrained devices in a batch, σ is tunable hyperparameter, $|p_f(\{\mathbf{r}_m\})|$ the total absolute pressure field at the focal point is given in vector form by Equation 2.14, $\boldsymbol{n}^{(\gamma)}$ are the gradients of the unconstrained devices with respect to the constrained device and the gradients $\boldsymbol{q}_j^{RMS}$ are computed analytically given by the Equation 2.19 in the vector form.

Following how the loss function is written, it is essential to tune the hyperparameters until the loss function converges to a range of numbers with minor fluctuations due to the non-linearity of the optimization problem considered. The trend of the loss function may follow the pressure amplitude throughout the training. The loss function calculates the gradients $\frac{\partial |p_f|^{RMS}}{\partial w}$ and further back-propagates to update the weights w.

3.4. 2D-GLOnets Results

3.4.1. Numerical Results for Acoustic Lens Design using 2D-GLOnets

In this section, we adopt ideas from [3], [9] and develop a machine learning framework to automate the acoustic lens design process by leveraging the capabilities of the 2D-GLOnets, DL, generative modeling, and gradient information. We consider rigid cylinders submerged in water with physical properties: density $\rho_0 = 1000 kg/m^3$ and the speed of sound $c_0 = 1480 m/s$. Based on the 2D-GLOnets model [7], [9] for acoustic cloak design, we have modified 2D-GLOnets for acoustic lens design. In the generative model, the objective function to maximize is the RMS of the absolute pressure amplitude at the focal point, i.e., $|p_f|^{RMS}$. In addition, the gradients of the RMS of the absolute pressure amplitude at the focal point with respect to positions evaluated in [3] and defined here by Equation 2.19, will be provided in these models to improve the training of generative models. The 2D-GLOnets generative model is implemented using PyTorch Python libraries calling the MATLAB engine from Python libraries and computing the objective function and its gradients with respect to positions in MATLAB [3].

3.4.2. Numerical Results for 2D-GLOnets at Lower Frequencies

In this section, we present numerical results for designing an acoustic lens using the 2D-GLOnets model for $N_k = 11$ discrete values of normalized wavenumbers $ka \in [0.35, 0.45]$ with an increment of 0.1 where $a = 1m$. The random noise vector is generated and passed to the 2D-GLOnets algorithms. The optimal results predicted by 2D-GLOnets are compared to ones produced by Global Optimization Toolbox using *MultiStart* solver combined with the *fmincon* nonlinear optimization solver initialized using the random positions of cylinders.

Fig. 9 illustrates 2D contour plots of total pressure fields at normal plane wave incidence on configurations $M = 7$ rigid cylinders at $ka = 0.40$. The lower figures show the real part of the total acoustic pressure field $\mathrm{Re}(p)$, and the bottom figures show the absolute value of the total acoustic pressure field $|p|$ for the random configuration (right figures), and configurations optimized by 2D-GLOnets (middle figures) and *fmincon* (left figures), correspondingly. The upper three plots are the real part of the total pressure $\mathrm{Re}(p)$ show how the plane waves interact with the configuration propagate through fluid media. The lower three plots are absolute pressure amplitude $|p|$ showing the magnitude of pressure amplitude. On the bottom figures, blue indicates low absolute pressure values, and yellow indicates high absolute pressure values. As the waves propagate horizontally from left to right at normal incidence, they interact with the acoustic lens and focus the wave energy on one point, which is called the focal point, denoted by an asterisk in the figures.

An example of the 2D-GLOnets outperforming *fmincon*, compares the 2D-GLOnets to *fmincon*, and non-optimized random configurations at $ka = 0.40$. The random configuration and configurations optimized by 2D-GLOnets and *fmincon* for $M = 7$ are depicted. The

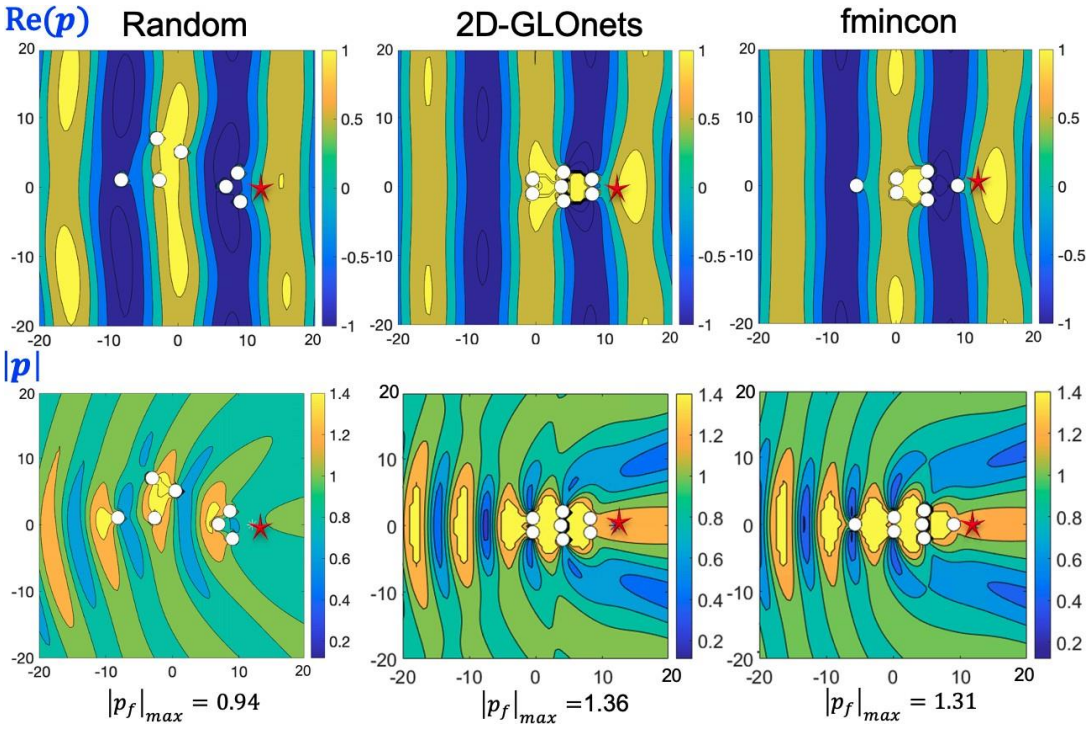

Fig. 9: Comparison of pressure fields between arbitrary random configuration (left column), 2D-GLOnets (middle column), and *fmincon* (right column). The variation of real part of total pressure, Re(p), (top figures) and absolute pressure amplitude, $|p|$, (bottom figures) at normal plane wave incidence on configurations of $M = 7$ rigid cylinders at $ka = 0.40$

asterisk denotes the location of the focal point (12, 0) on the plots. The 2D-GLOnets and *fmincon* show similar optimized patterns where the scatterers are symmetrical to the x-axis. The pressure fields are plotted for visualization of focusing effect. The total absolute pressure amplitude $|p|$ and real part of the total pressure Re(p) are plotted.

The corresponding loss function and absolute pressure amplitude v.s. number of epochs are depicted in Fig. 10 at $ka \in [0.35,\ 0.45]$ for $M = 7$. As illustrated in Fig. 10(a), the optimized absolute pressure amplitude of the 2D-GLOnets converges to $|p_f| \approx 1.36$, which surpasses the optimized absolute pressure amplitude $|p_f| = 1.32$ by *fmincon*. From Fig. 10(b), one can notice the loss function has fluctuations. Due to the way the loss function is written,

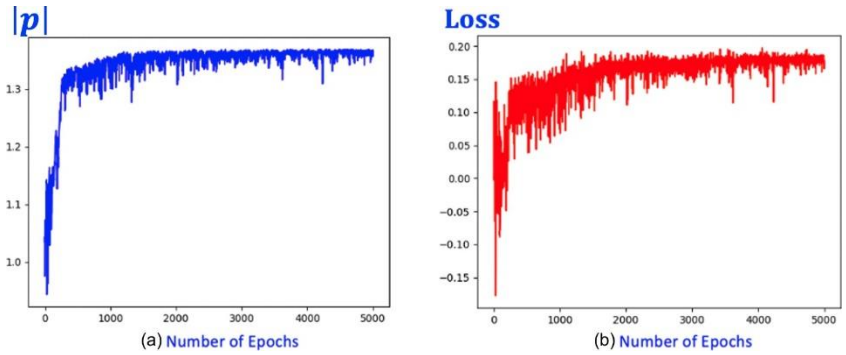

Fig. 10: The variation of absolute pressure amplitude $|p|$ (left) and loss function (right) v.s. number of epochs using the 2D-GLOnets for $M = 7$ at $ka \in [0.35,\ 0.45]$

as long as the loss function converges to a range of numbers, it is considered acceptable. The absolute pressure amplitude plot Fig. 10(a) shows a converging trend with a decreasing variance as the number of epochs increases.

Fig. 11 shows the absolute pressure amplitude with a varying number of cylinders. The absolute pressure amplitudes at the focal point for $M = 8, 9,\ 11$, and 12 scatterers were plotted. These four examples are ones where the performance of the 2D-GLOnets is better than that of *fmincon*. The focusing effects are shown. A pattern of symmetry about the x-axis is observed with a varying number of cylinders at lower frequencies for both 2D-GLOnets and *fmincon* results.

3.4.3. Results at Higher Frequencies for 2D-GLOnets

Fig. 12 depicts comparison between random configuration (left) and optimized configurations: 2D-GLOnets (middle), *fmincon* (right) with $M = 9$ at high frequencies $ka \in [1.35,\ 1.45]$. $Re(p)$ is the real part of total pressure, and $|p|$ is the absolute pressure amplitude. The optimized configuration of the cylinders becomes more scattered. This example shows that the 2D-GLOnets produces $|p|_{max} = 2.28$, and it outperforms the *fmincon*

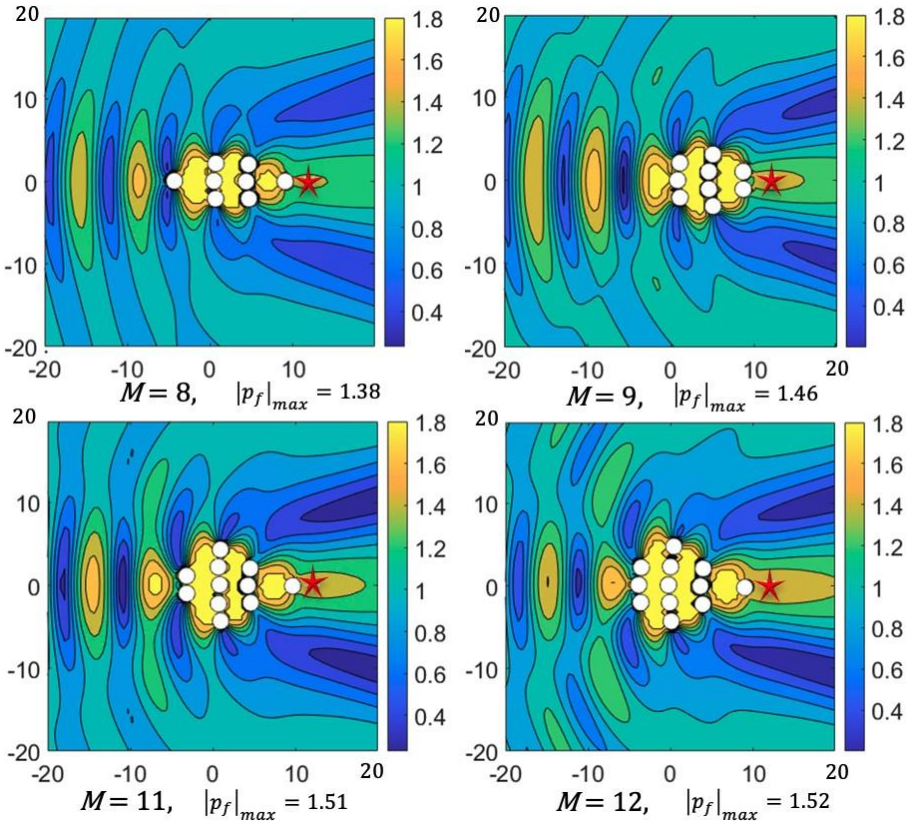

Fig. 11: 2D-GLOnets optimized results for the absolute pressure field $|p|$ with M = 8, 9, 11, and 12 at ka = 0.40.

solver that produces $|p|_{max}$ = 2.07. Contrary to the random configuration, the 2D-GLOnets model produces distinct focusing effects at the focal point, as denoted with an asterisk in Fig. 12.

Fig. 13 shows the training curve in (a) and loss function in (b) as a function of epochs whose optimized configuration is previously shown to be in the middle column of Fig. 12. The batch size U used is 15. It is noticed that the absolute pressure amplitude at the focal point fluctuates towards the beginning of the training. One can notice that the absolute pressure suddenly goes down and back up to a converged value because the 2D-GLOnets can get out of local minima to find the global maxima. The loss function successfully converges

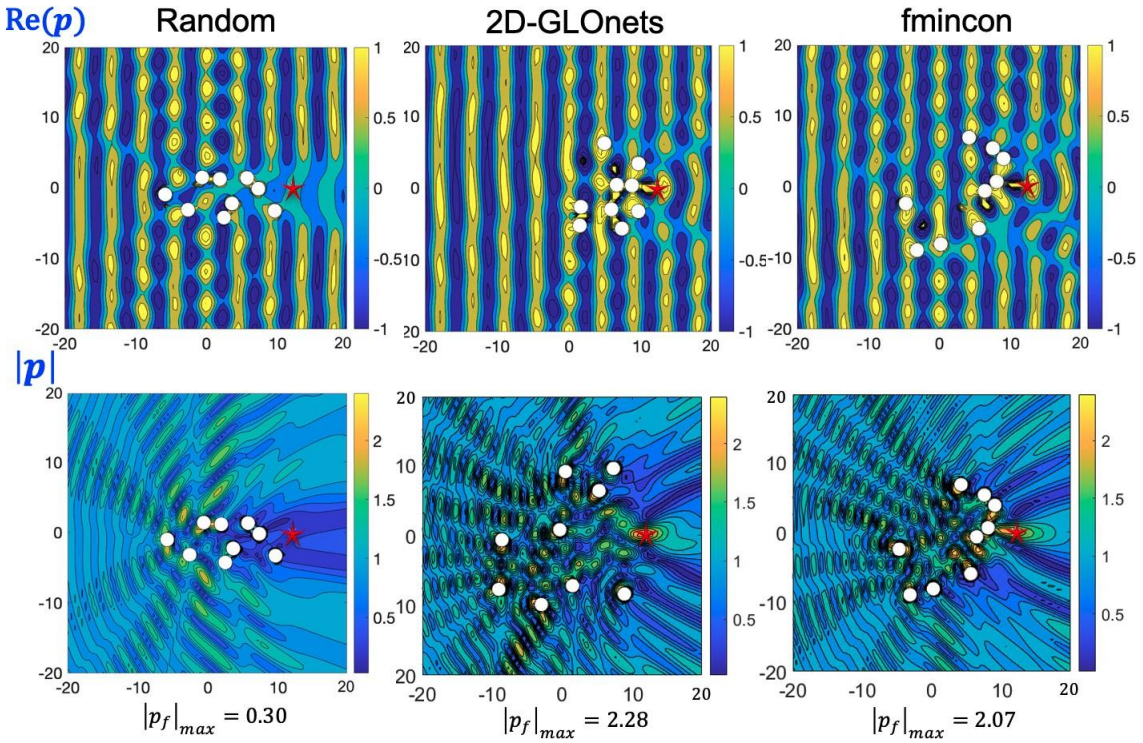

Fig. 12: Comparison of pressure fields between arbitrary random configuration (left column), 2D-GLOnets (middle column), and *fmincon* (right column) at $ka = 1.40$. Real part of total pressure, Re(p), (top figures) and absolute pressure amplitude, $|p|$, (bottom figures) at normal plane wave incidence on configurations of $M = 9$ rigid cylinders $ka = 1.40$.

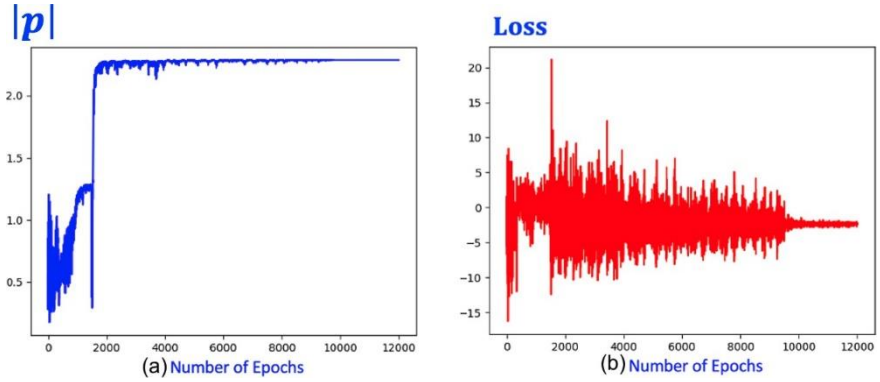

Fig. 13: The variation of absolute pressure amplitude $|p|$ (left) and loss function (right) v.s. number of epochs using 2D-GLOnets for $M = 9$ at $ka \in [1.35,\ 1.45]$

after oscillating. Towards the end of the training, the noise in the absolute pressure and the loss function reduce significantly after approximately the 9500th epoch.

Fig. 14 presents the 2D-GLOnets results of absolute total pressure amplitude $|p|$ for M = 7, 8, 10, and 11 at a selected wavenumber ka = 1.40. Note that the absolute pressure of the normal incident wave is $|p_{inc}|$ = 1.0. These four examples illustrate the performance of optimized configurations which outperform *fmincon*. The focusing effects are observed at the focal point denoted as an asterisk. The absolute pressure field at the high-frequencies range is the clear sound localization and focusing effects.

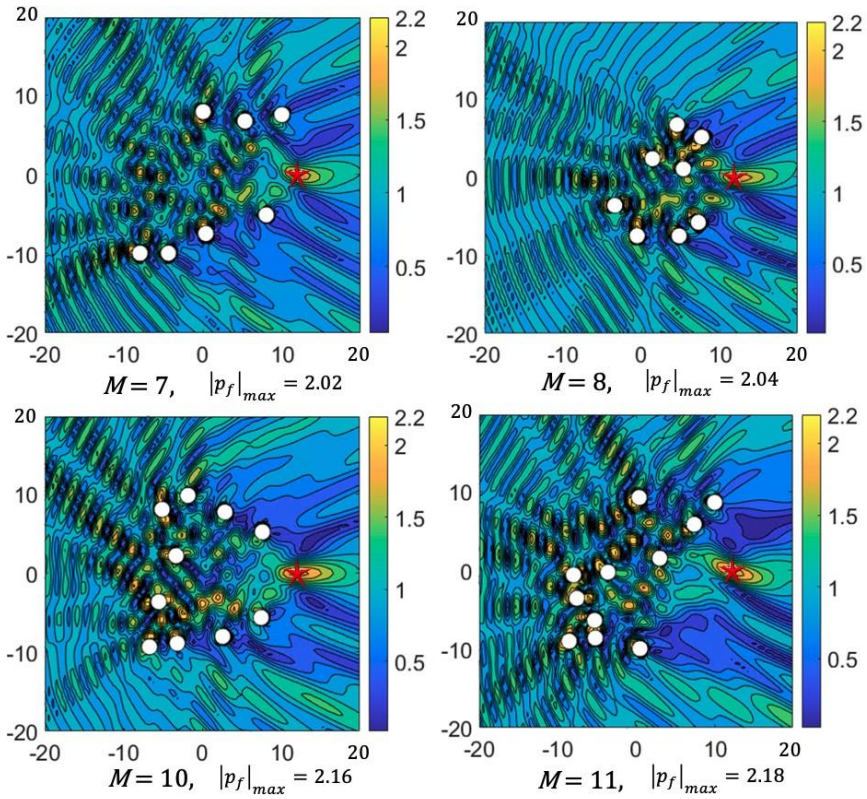

Fig. 14: The absolute value of the total acoustic pressure field $|p|$ for the optimized configurations of M = 7, 8, 10, and 11 optimized by 2D-GLOnets at ka = 1.40

All the four optimized configurations outperform *fmincon* results producing the following $|p_f|$ tabulated in Table 3.

Table 3: Numerical Results of Performance Comparison Between 2D-GLOnets and *fmincon*

	2D-GLOnets	*fmincon*		2D-GLOnets	*fmincon*
$M = 7$	2.08	1.95	$M = 8$	1.98	1.89
$M = 10$	2.12	1.91	$M = 11$	2.14	2.09

Fig. 15 depicts examples of the absolute value of the total acoustic pressure fields $|p|$ that are outside the optimized wavenumber range, i.e., $ka \in [1.35, 1.45]$. The numbers of scatterers of $M = 8$ (left column) and $M = 10$ (right column) are considered for $ka = 1.45$, 1.5, and 1.6, which are outside the optimized wavenumber range. The middle row figures show that that lens devices still produces focusing effect at wavenumber at $ka = 1.5$ which is outside the range at which the device was optimized. As the wavenumber *ka* increases further, the focusing effects are diminishing as expected.

3.4.4. Numerical Results for Broadband Acoustic Lens Design

For broadband acoustic lens design, the objective is to maximize the absolute pressure amplitude at the focal point. To validate 2D-GLOnets results and analyze its performance, MATLAB *fmincon* solver was used to find the maximum of the nonlinear non-convex objective function, i.e., absolute total pressure at the focal point $|p_f|$.

We performed simulations running *fmincon* on MATLAB and validated numerical results obtained by the 2D-GLOnets [3]. The initial configuration and final acoustic lens configuration for $ka \in [0.35,\ 0.45]$ and $ka \in [1.35, 1.45]$ are shown in Fig. 16 and Fig. 17,

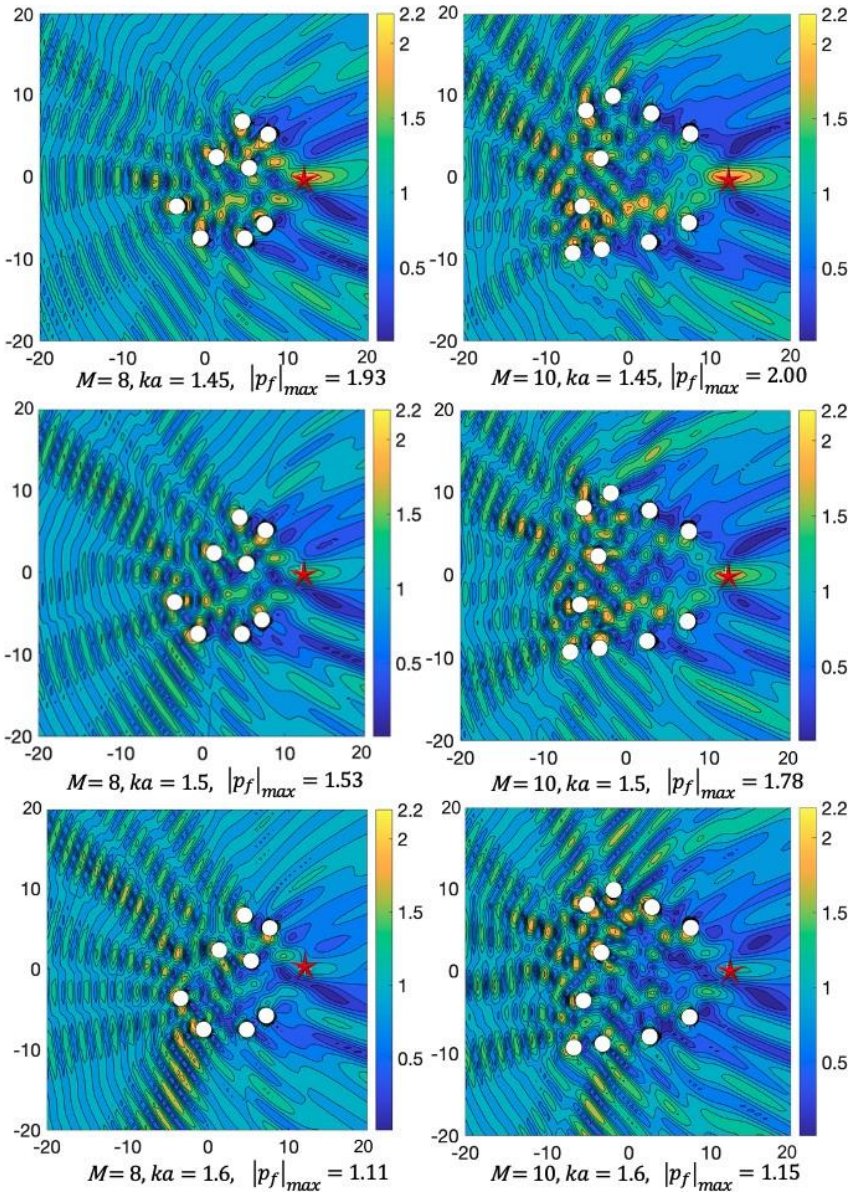

Fig. 15: The absolute value of the total acoustic pressure fields $|p|$ for $M = 8$ (left column) and $M = 10$ (right column) with $ka = 1.45$ (upper row), $ka = 1.5$ (middle row), and $ka = 1.6$ (bottom row) are shown. The wavenumbers ka considered are outside the optimized wavenumber range, i.e., $ka \in [1.35, 1.45]$. The configurations used to plot the 6 figures are the 2D-GLOnets optimized configurations at $ka \in [1.35, 1.45]$.

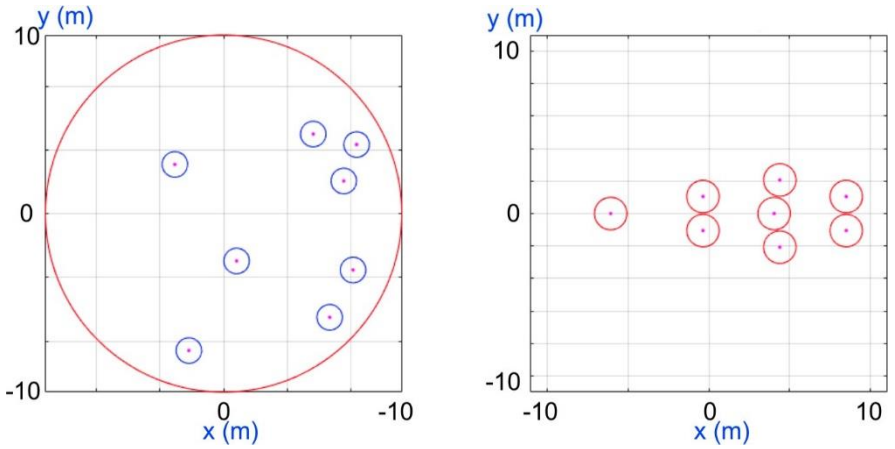

Fig. 16: A random configuration (left figure) using pressure amplitude function. *Fmincon* optimized acoustic lens configuration of M = 8 scatterers (right figure) for $ka \in [0.35, 0.45]$.

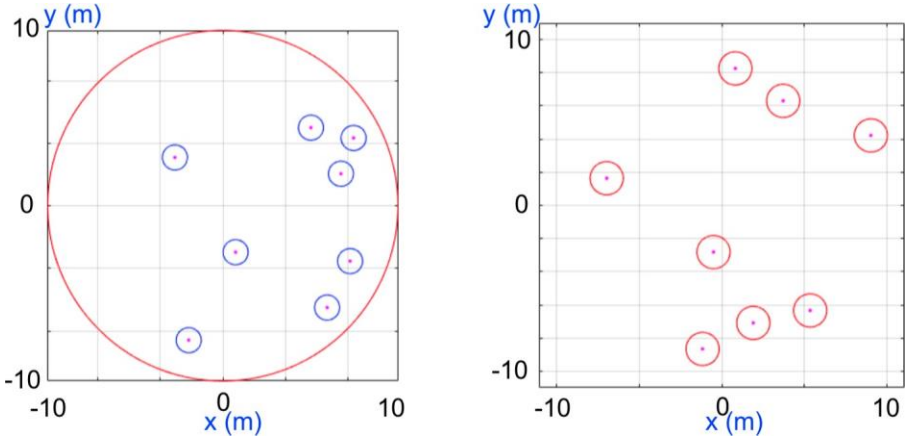

Fig. 17: A random configuration (left figure) using pressure amplitude function. *Fmincon* optimized acoustic lens configuration of M = 8 scatterers (right figure) for $ka \in [1.35, 1.45]$.

respectively. The acoustic lens design enables the pressure amplitude to be maximized at the focal point. The maximized absolute pressure amplitudes for $ka \in [0.35, 0.45]$ and $ka \in [1.35, 1.45]$ are $|p_f| = 1.40$ and $|p_f| = 2.10$, respectively. The total pressure field and absolute pressure field are plotted to show the focusing effect with a focal point of (12, 0), which is

pre-designed. The plane waves with an incident angle of 0 degrees propagate from left to right, in positive *x*-direction.

3.4.5. Dependency of Absolute Pressure Amplitude on wavenumber ka at a Range of Wavenumbers

3.4.5.1. 2D-GLOnets Low Frequency Analysis

In this section, we will show broadband performance of acoustic lenses which produce sound localization and focusing effects at range of wavenumbers within and outside the ranges at which the objective function was optimized. We will consider two ranges of wavenumbers $ka \in [0.35,\ 0.45]$ and $ka \in [1.35,\ 1.45]$. The RMS absolute pressure amplitude at the focal point is optimized at $ka \in [0.35,\ 0.45]$ for the configurations of $M = 6,\ 8,\ 10$, and 12 cylinders at plane wave incidence. Fig. 18 shows the variation of absolute pressure at the focal point $|p_f|$ with wavenumber *ka* at low values of $ka \in [0.35, 0.45]$. We compare the 2D-GLOnets results to *fmincon* results. As expected, the absolute pressure amplitude of the non-optimized configurations depicted by green color appears to be much lower than the 2D-GLOnets shown by blue curve lines and *fmincon* indicated by the green curves at $ka \in [0.35, 0.45]$. The 2D-GLOnets results are comparable with *fmincon* results at the optimized wavenumber region, i.e., $ka \in [0.35,\ 0.45]$. It is noticed that for $M = 6$ and $M = 10$ at $ka \in [0.35, 0.45]$, 2D-GLOnets performed similarly to *fmincon*. whereas for $M = 8$ and $M = 12$, 2D-GLOnets underperformed slightly compared to *fmincon*.

Fig. 19 shows the variation of absolute pressure amplitude at focal point $|p_f|$ with wavenumber *ka* at low values of $ka \in (0.00, 1.00]$. The absolute pressure amplitudes at focal point $|p_f|$ of *fmincon* results drawn by the red curve, 2D-GLOnets results drawn by the blue

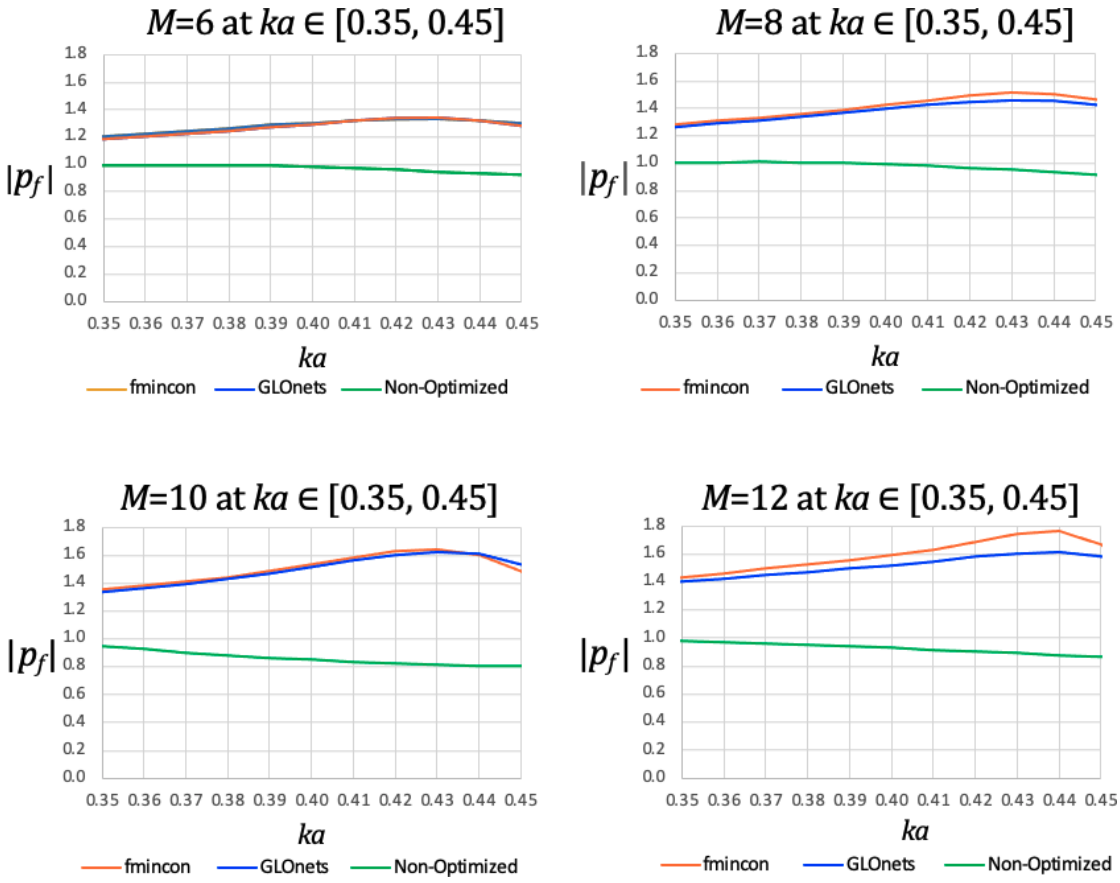

Fig. 18: The dependency of absolute pressure amplitude with $ka \in [0.35, 0.45]$ at lower wavenumbers for various fixed numbers of scatterers $M = 6$, 8, 10, and $M = 12$. Here, the red curve corresponds to *fmincon* results, the blue curve is 2D-GLOnets results, and the green curve represents results for non-optimized random configuration of scatterers and is given a reference for comparison.

curve, and non-optimized results drawn by the green curve are shown. The behavior of pressure amplitude becomes more complex outside the optimized frequency regions. At $ka \in (0.00, 0.20]$, all the three configurations' pressure amplitudes overlap in general. At around $ka = 0.20$, the pressure amplitude jumps up. At $ka \in [0.45, 1.00]$, the pressure amplitude of 2D-GLOnets and *fmincon* will go lower compared to the non-optimized configuration.

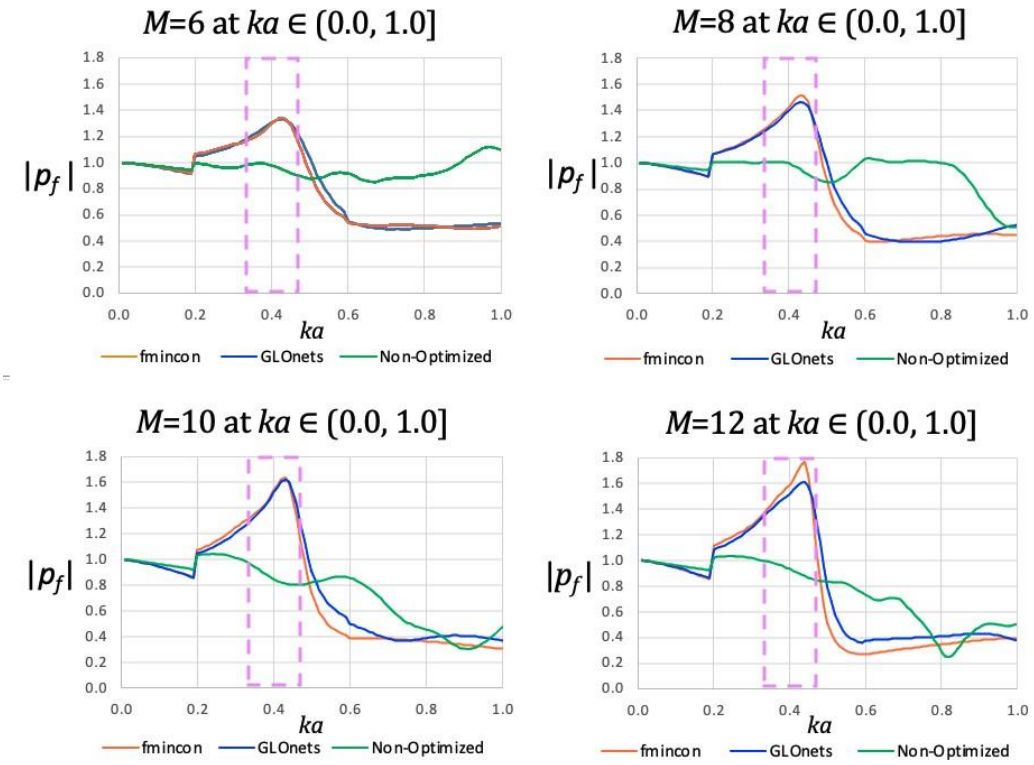

Fig. 19: The dependency of absolute pressure amplitude with $ka \in (0.00, 1.00]$ at lower wavenumbers for various fixed numbers of scatterers $M = 6$, 8, 10, and $M = 12$. The optimized region, i.e., $ka \in [0.35, 0.45]$ is colored in pink. Here, the red curve corresponds to *fmincon* results, the blue curve is 2D-GLOnets results, and the green curve represents results for non-optimized random configuration of scatterers and is given a reference for comparison.

3.4.5.2. 2D-GLOnets High Frequency Analysis

Fig. 20 shows the behavior of absolute pressure amplitude at the focal point $|p_f|$ for 2D-GLOnets (blue curve), *fmincon* (red curve), and the non-optimized (green curve) configurations at the optimized region, i.e., $ka \in [1.35, 1.45]$. For $M = 8$ and $M = 10$, the 2D-GLOnets outperform *fmincon*. Whereas, for $M = 6$ and $M = 12$, the 2D-GLOnets underperform *fmincon*. The 2D-GLOnets and *fmincon*'s pressure amplitudes $|p_f|$ go higher substantially compared to the non-optimized design, as the 2D-GLOnets and *fmincon* optimize the design.

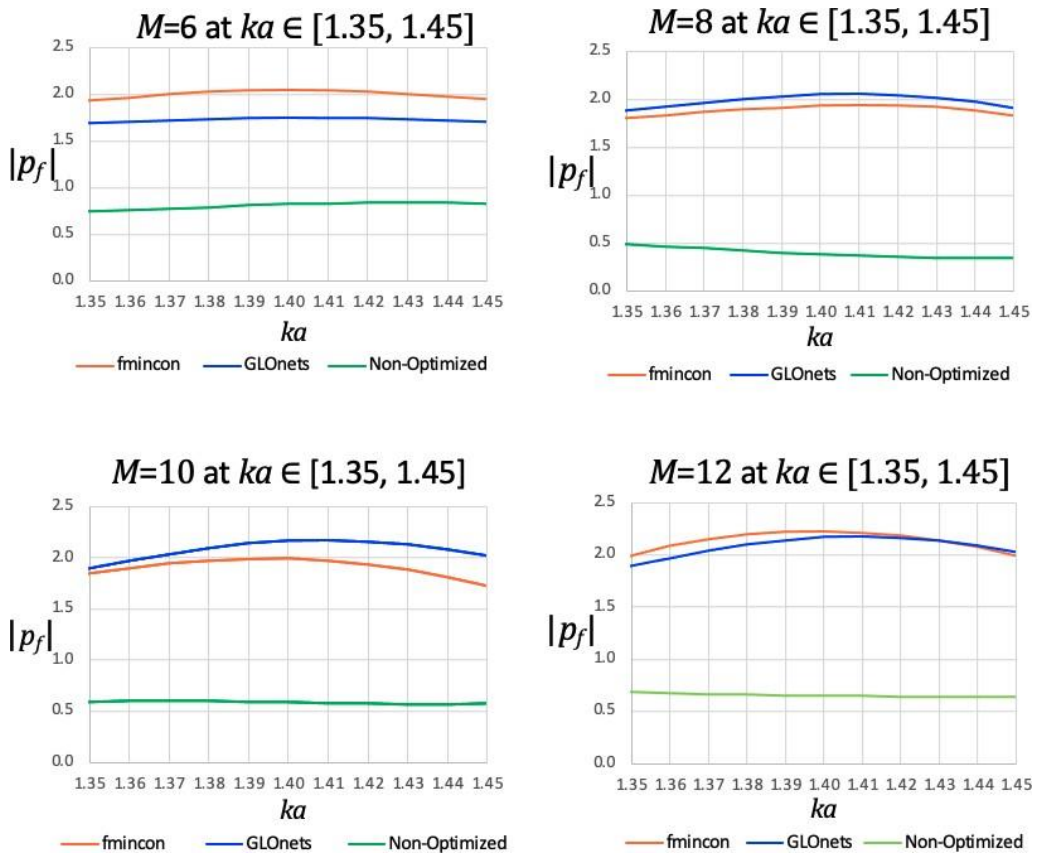

Fig. 20: The dependency of absolute pressure amplitude with $ka \in [1.35, 1.45]$ at higher wavenumbers. Here, the red curve indicates *fmincon* results, the blue curve depicts 2D-GLOnets results, and the green curve indicates results for non-optimized random configuration of scatterers.

To investigate the behavior of absolute pressure amplitude at the focal point $|p_f|$ outside the optimized region, Fig. 21 is plotted for $ka \in (0, 2]$. When ka is close to zero, i.e., $ka \in (0.00, 0.10]$, the behavior of all the three configurations is almost identical. Nevertheless, the pressure amplitude function gets more complex approximately at $ka \in (0.10, 1.25]$. At $M = 6$ and $M = 8$, the pressure amplitude for the non-optimized design is low in contrast with the 2D-GLOnets and *fmincon*.

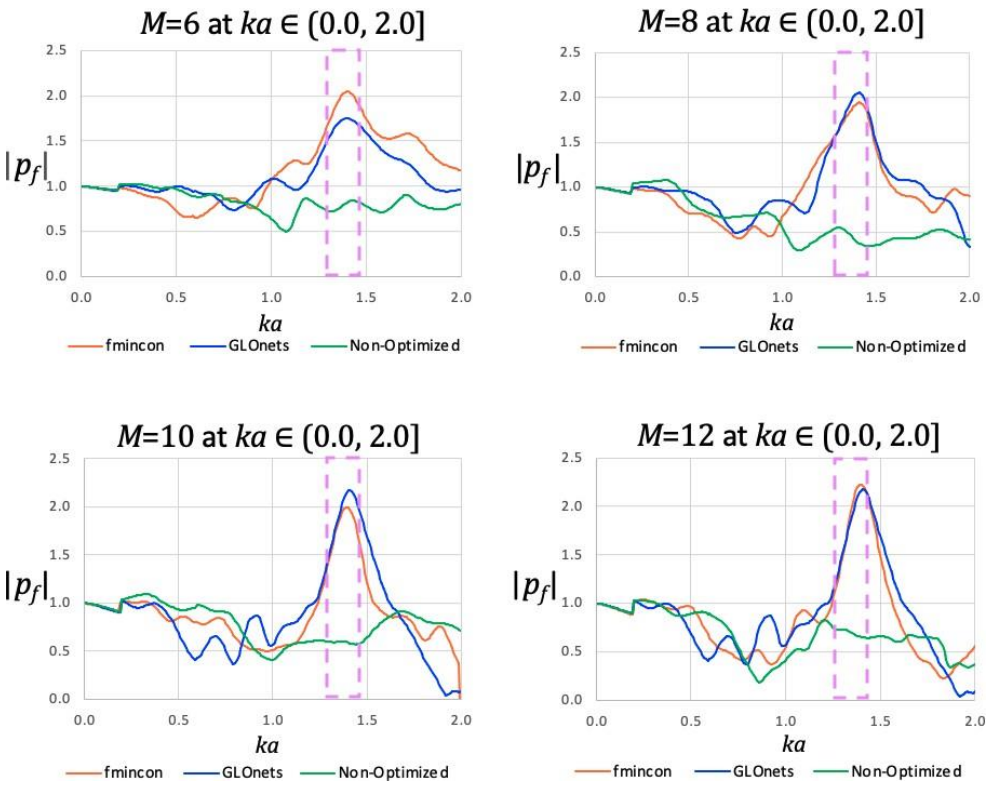

Fig. 21: The dependency of absolute pressure amplitude with $ka \in (0.00, 2.00]$ at higher wavenumbers varying the numbers of scatterers $M = 6$, 8, 10, and $M = 12$. The optimized region, i.e., $ka \in [1.35, 1.45]$ is colored in pink. Here, the red curve indicates *fmincon* results, the blue curve shows 2D-GLOnets results, and the green curve denotes results for non-optimized random configuration of scatterers and is given a reference for comparison.

3.5. Discussion for 2D-GLOnets Model

We proposed the 2D-GLOnets implementation of broadband acoustic lens design. Importantly, the 2D-GLOnets were capable of outperforming *fmincon* solver, which uses state-of-the-art optimization algorithms, such as sequential quadratic programming (SQP) algorithms. Analytical gradients in the loss function assist devices in moving toward an optimal region. The significant results of the 2D-GLOnets are listed as follows:

– The 2D-GLOnets results show focusing effects using up to 12 cylinders.

- We observed that when properly tuned, the 2D-GLOnets achieve convergence and can identify global maxima.
- We have shown some cases where the 2D-GLOnets optimized pressure amplitude is comparable to or higher than *fmincon*.
- The 2D-GLOnets results have a pattern of symmetry along the *x*-axis in the low-frequency range.
- The 2D-GLOnets results have no distinct patterns in the high-frequency range.

With the current development, the 2D-GLOnets and *fmincon* start from different configuration because the 2D-GLOnets has a Gaussian noise vector as an input to the generator. Similarly, the *fmincon* and *MultiStart* solvers consider multiple devices choosing the same number of scatterers. The *MultiStart* solver with *fmincon* considers the number of scenarios, e.g., 100, which was used in the 2D-GLOnets model. Due to reparameterization step, the current implementation of the 2D-GLOnets requires large memory in GPUs, which reduces the batch size with an increase of number of scatterers *M*. Therefore, to perform a proper comparison between 2D-GLOnets and *MultiStart*, we modified batch size and number of scatterers accordingly.

Each scenario has been run by using the 2D-GLOnets a few times until the pressure amplitude approaches a value to ensure hyperparameter tuning stability. Therefore, even though the comparison is not directly due to randomness in the initial configuration, we have seen the promising results of applying the 2D-GLOnets to our acoustic lens design problem.

One of the most significant benefits of using the 2D-GLOnets model is to design acoustic lenses with large amounts of scatterers. However, we have not had sufficient computational

resources to accommodate more cylinders due to reparametrization procedure. We discuss how to overcome this issue in Chapter 6: Future Work.

4. REINFORCEMENT LEARNING ASSISTED BROADBAND ACOUSTIC LENS DESIGN

4.1. Reinforcement Learning

RL is one of the critical areas of machine learning technology that allows agents to learn by trial and error in an interactive environment utilizing feedback from behaviors and experiences. RL includes Q-learning [112] and policy gradient [96]. In RL, an agent chooses actions and learns from rewards while interacting with the environment. The environment is where the agent operates, and the state is the current situation of the agent. Data are produced simultaneously as the interaction between the agent and the environment progresses. The policy will be improved as the agent learns.

4.1.1. The Markov Decision Process (MDP)

The Markov Decision Process (MDP) is a discrete-time stochastic control process. The states are partially randomized and partially controlled by an agent. Fig. 22 shows the interaction between an agent and an environment in an MDP. The future action is dependent on the current action. The agent interacts with the environment over time. At time t, the agent receives a state S_t and selects an action A_t. Consequently, the agent receives a reward R_{t+1} and transitions to the next state S_{t+1}. The aforementioned process allows the episode to proceed until it reaches a terminal state. The representation of an episode trajectory is given by S_0, A_0, R_1, S_1, A_1, R_2, S_2, A_2, R_3, ... [5].

In most cases, the objective of RL is to maximize the cumulative reward in an epoch [113]. The reward equation is given by

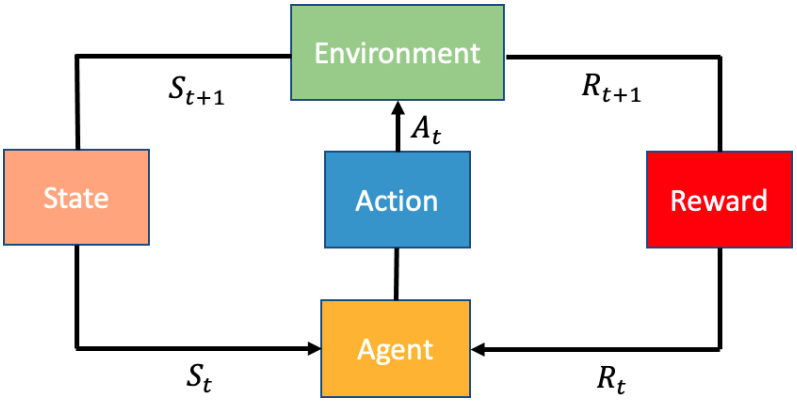

Fig. 22: Agent-environment interaction in an MDP

$$G_t \doteq \sum_{k=t+1}^{T} R_k, \tag{4.1}$$

where T is the terminal time, and R_k is the reward.

It is typical for RL algorithms to train an action-value function Q^* to obtain an estimation of G_t. The Bellman Equation is given below [5]:

$$Q_*(s,a) = E[R_{t+1} + \gamma \max_a Q_*(S_{t+1}, a) | S_t = s, A_t = a], \tag{4.2}$$

which decomposes the value function into immediate reward and the discounted future values, helps find the maximum policy and solves the Markov Decision Process. Starting with a state-action pair (s, a) at time t with the optimal policy, the expected reward R_{t+1} at time $t + 1$ will be obtained. Furthermore, maximizing the expected discounted return is attainable for any upcoming state-action pair (s', a'). Consequently, the RL algorithm can find the action that maximizes $Q^*(s, a)$ to search for the optimal Q-value through a recursive process.

4.1.2. Deep Deterministic Policy Gradient (DDPG)

The DDPG [96], [97], [114], whose architecture is shown in Fig. 23 is a model-free algorithm that employs off-policy actor-critic techniques. It integrates Q-learning and policy gradients. An agent explores continuous action space as it interacts with an environment. RL uses experience replay to store the experiences of an agent at each time step. Our current DDPG model shown in Fig. 23 utilizes the deep neural networks that randomly samples a mini-batch of experiences to learn off-policy. Compared with uniform sampling, the DDPG with prioritized experience replay achieves better results regarding training time and stability [97]. The source code of the DDPG model is located at [115].

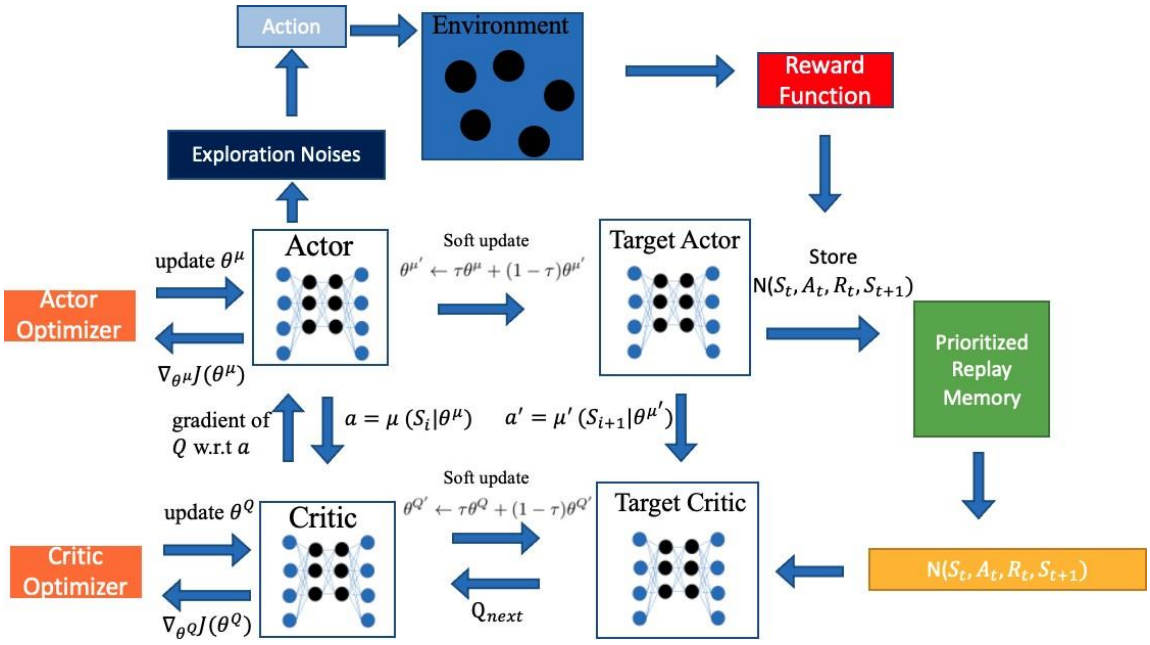

Fig. 23: DDPG structure: A basic framework for DDPG illustrating how an agent interacts with the environment. It shows actor, target networks, critic, critic networks, and the reward function. Most importantly, prioritized replay memory is used in the DDPG networks.

Positional adjustments are made to move each scatterer by ±a unit in the x-direction and by ±a unit in the y-direction. Therefore, if there are M cylinders, 4M actions are selected. The

actor, critic, target actor, and target critic are networks used by DDPG. Target networks help with the stability of the training. The actor's input is the state, and its output is the continuous action without utilizing a probability distribution over actions. The critic's input is the state and action pair (*s, a*), and its output is the Q-value prediction *Q* (*s, a*). The actor and critic networks' approximators are θ^{μ} and θ^{Q}, respectively [116]. The target networks are updated using the soft updates strategy. Since implementing Q learning renders the training unstable, a soft update can solve this issue. The actor and critic target networks are copies of the actor and critic networks, respectively. The actor target networks is updated by $\theta^{\mu'} \leftarrow \tau\theta + (1 - \tau)\theta^{\mu'}$. The critic target networks is updated by $\theta^{Q'} \leftarrow \tau\theta + (1 - \tau)\theta^{Q'}$ [117]. The soft target update parameter τ is set to 0.001 following Lillicrap et al. [96]'s suggestion. Therefore, the target values are limited to slow change, ensuing the training stability [96].

The reward function for the RL model of acoustic lens design problems is formulated by the piece-wise function below:

$$R = \begin{cases} |p_f|_t^{RMS} & \text{for legal state,} \\ |p_f|_{t-1}^{RMS} - 1 & \text{for illegal state.} \end{cases} \tag{4.3}$$

The reward function is given by the RMS absolute total pressure amplitude at the focal point $|p_f|^{RMS}$ to raise the pressure amplitude at the focal point $|p_f|^{RMS}$. The legal state requires that the non-overlapping constraint be satisfied. If violated, a penalty will be assigned to the reward function at the previous state.

The DDPG model for acoustic cloak was implemented by Shah et al. [6] and Zhuo [7] initially using Python PyTorch libraries calling the MATLAB engine from Python libraries.

Nevertheless, It was computationally expensive because the MATLAB engine had to be called each time the RMS of the pressure amplitude was computed. Therefore, Julia was used to implement RL model to maximize the pressure amplitude function. As a result, the Julia-based RL model framework reduces computation time by at least 20 times compared to the Python-MATLAB implementation. The current Julia implementation of the DDPG model does not use the gradient information but can be included to improve convergence speed [6]. The DDPG hyperparameters are tabulated in Table 4.

Table 4: DDPG Hyperparameter Table

Hyperparameters	**Values or functions**
Batch size U	1024 (low frequencies); 128 (high frequencies)
Discount factor γ	0.9
How aggressive prioritized sampling probability gets corrected β	0.5
Activation function between layers	*ReLU*
Optimizer	*Adam*
Target update factor τ	0.001
Target update rate (number of episodes per epoch)	30, 000
Learning rate for the actor	0.0001
Learning rate for the critic	0.001
Number of hidden neurons for the actor	128
Number of hidden neurons for the critic	128
Number of layers for the actor	2
Number of layers for the critic	2
Critic weight decay	0.01
Memory size	1, 000, 000

4.2. Numerical Results for Acoustic Lens Design Using Reinforcement Learning

4.2.1. Lower Frequency Results for RL Model

Fig. 24 shows non-optimized random (left column), RL (middle column), and *fmincon* (right column) results at low frequencies. The focal point is denoted by an asterisk. Both real part of pressure amplitude *Re*(*p*) and absolute pressure amplitude |*p*| are shown in the upper and lower part, respectively. Both *fmincon* and RL start from the same random configuration. *MultiStart* solver is not utilized. The RL model was trained for M = 2,3, 4,5, and 6 for lower wavenumbers $ka \in [0.35, 0.45]$. As illustrated in Fig. 24, the optimized configuration predicted by the RL model shows a sub-optimal solution for acoustic lens design with 6 scatterers whose optimized pressure amplitude is still lower than *fmincon*.

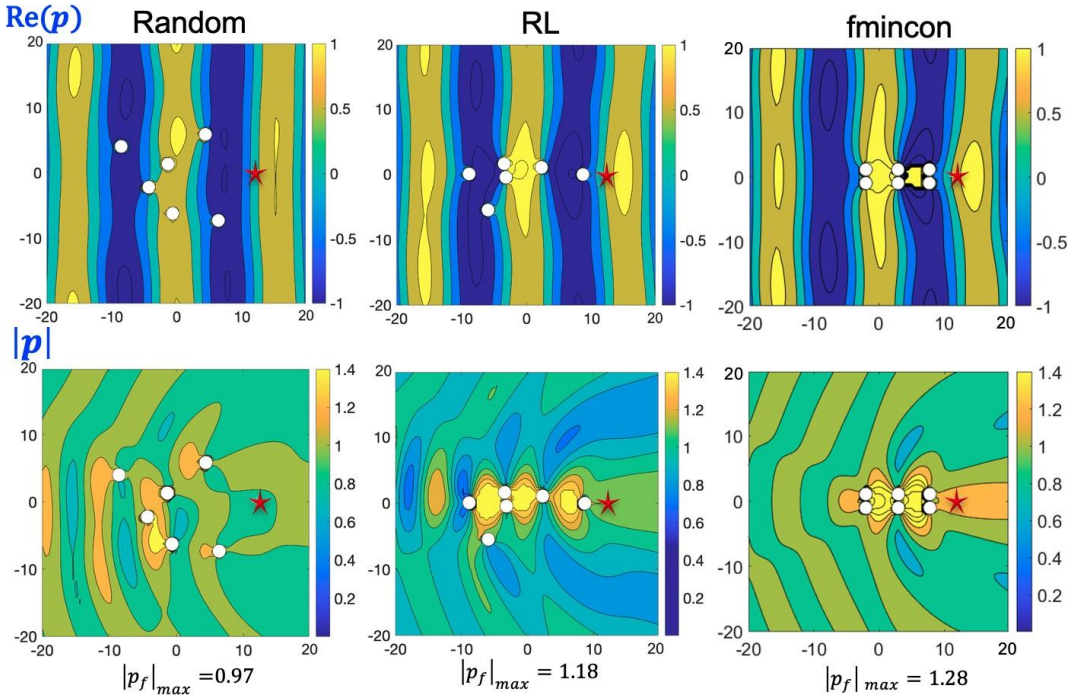

Fig. 24: The variation of real part of total pressure Re(*p*) (top figures) and absolute pressure amplitude |*p*| (buttom figures) at normal plane wave incidence on configurations M = 6 rigid cylinders at ka = 0.40, for arbitrary random configuration (left column), RL (middle column), and *fmincon* (right column).

The training curve for $M = 6$ is shown in Fig. 25 to illustrate the absolute pressure amplitude at the focal point at $ka \in [0.35, 0.45]$. The DDPG model explores different maxima until the convergence of the absolute pressure is achieved. The number of episodes in an epoch is increased to 30, 000 in one epoch to obtain better performance using the grid search method, which results in a substantial time increase. The optimized absolute pressure amplitude of the RL converges to $|p_f| \approx 1.18$. The cumulative reward of DDPG plotted at each epoch in Fig. 26 converges as well. The magnitude of the reward is due to a great number of episodes per epoch during the training.

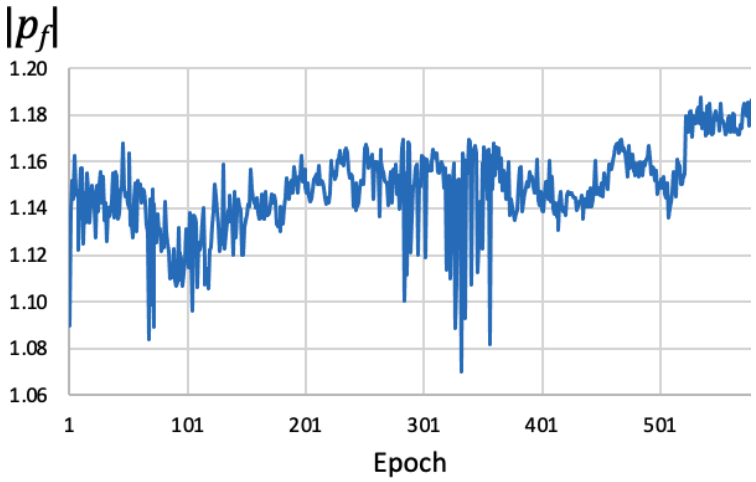

Fig. 25: DDPG training curve v.s. epochs for $M = 6$ at $ka \in [0.35, 0.45]$

The results of the absolute pressure amplitude with a varying number of cylinders at low values of wavenumbers $ka \in [0.35, 0.45]$ are shown in Fig. 27. Results for configurations of $M = 2$, 3,4, and 5 were plotted at $ka = 0.4$. After hyperparameters tuning, a large batch size of 1024 is utilized for training the model to perform better. The absolute pressure amplitudes for $M = 2$, 3, 4, and 5 are 1.06, 1.10, 1.15, and 1.18, respectively. As the number of cylinders M

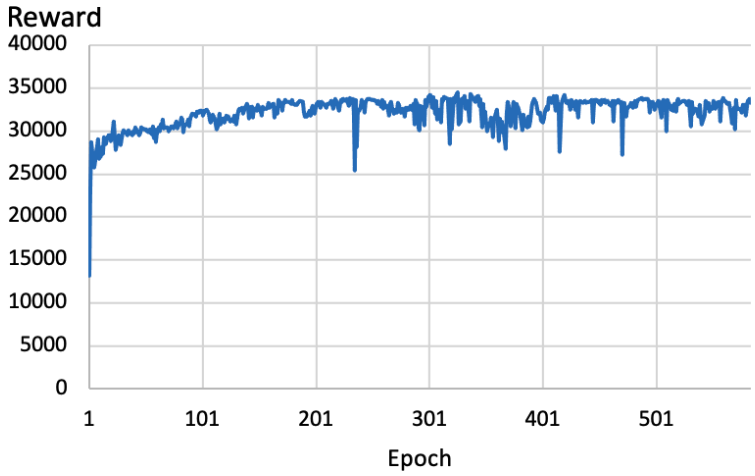

Fig. 26: Cumulative reward for $M = 6$ at $ka \in [0.35, 0.45]$

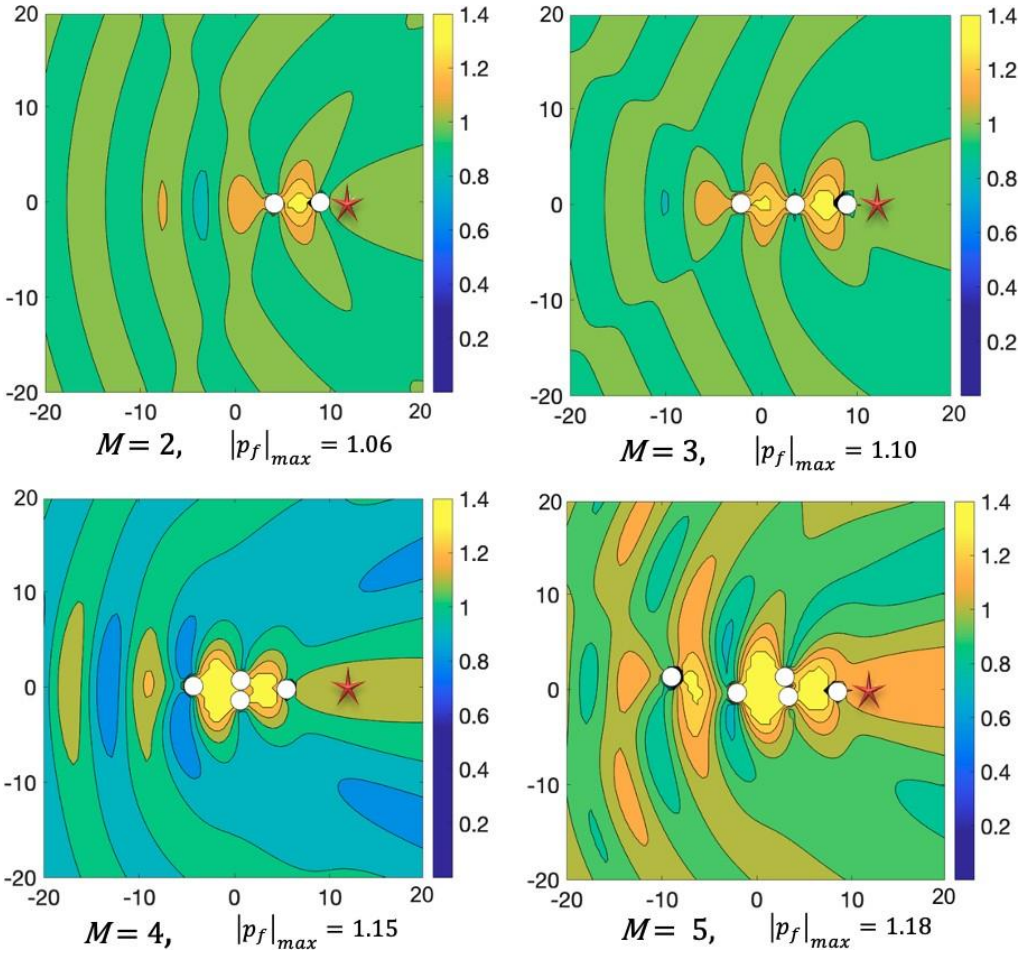

Fig. 27: DDPG results for the absolute total pressure field with $M = 2, 4, 5, 6$ at $ka = 0.40$

increases, the DDPG produces sub-optimal solutions compared to *fmincon*, and the focusing effects become better.

4.2.2. Higher Frequency Results for RL Model

At higher frequencies, the DDPG model was trained for M = 2, 3, 4, 5, 6, 8, 10, 12, 14, and 16. It is easier for DDPG to optimize the design at higher frequencies. The number of scatterers used by RL is greater than that used by 2D-GLOnets at normalized wavenumbers $ka \in [1.35, 1.45]$. Fig. 28 shows the absolute pressure amplitude $|p|$ and real part of the total pressure $Re(p)$ for random (left), RL (middle), and *fmincon* (right) configuration for M = 14. The absolute total pressure amplitude $|p|$ for RL, *fmincon*, and random at the focal point is $|p|$ = 1.79, 1.85, and 0.26, respectively. It is observed that RL's scatterers are located around the square geometric boundaries, i.e., $x \in [-10, 10]$ and $y \in [-10,10]$, whereas *fmincon*'s scatterers are more scattered within the boundaries.

Fig. 29 depicts the training curve that consists of the absolute pressure absolute $|p|$ v.s. number of epochs. $|p|$ converges around 1.8. Fig. 30 shows the cumulative reward for M = 14 at higher frequencies range. At the beginning of the training, adverse actions are taken, resulting in negative cumulative rewards. Afterwards, the cumulative reward per epoch gets positive and eventually oscillates around 5,000.

Fig. 31 represents the RL optimized configurations for M = 6, 8, 12, and 14 at higher frequencies at $ka \in [1.35, 1.45]$. The absolute total pressure amplitude $|p|$ at ka = 1.40 for M = 6, 8, 12, and 14 is $|p|$ = 1.92, 1.93, 1.81, and 1.82, respectively. The focusing effects are

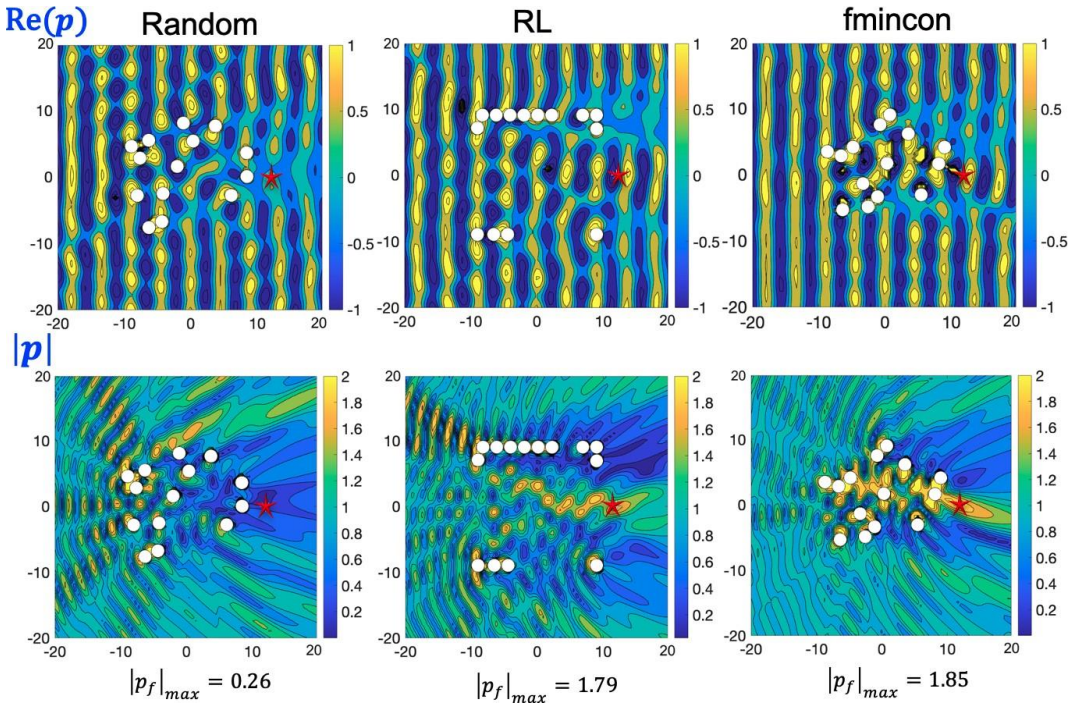

Fig. 28: Comparison of pressure fields between arbitrary random configuration (left column), RL (middle column), and *fmincon* (right column) at ka = 1.40. Real part of total pressure, Re(p), (top figures) and absolute pressure amplitude, $|p|$, (bottom figures) at normal plane wave incidence on configurations of M = 14 rigid cylinders ka = 1.40.

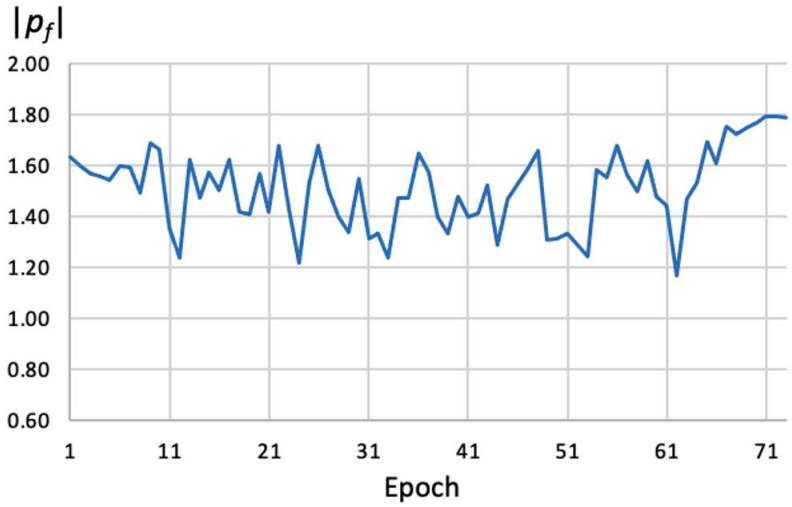

Fig. 29: DDPG training curve v.s. epochs for M = 14 at $ka \in$ [1.35, 1.45]

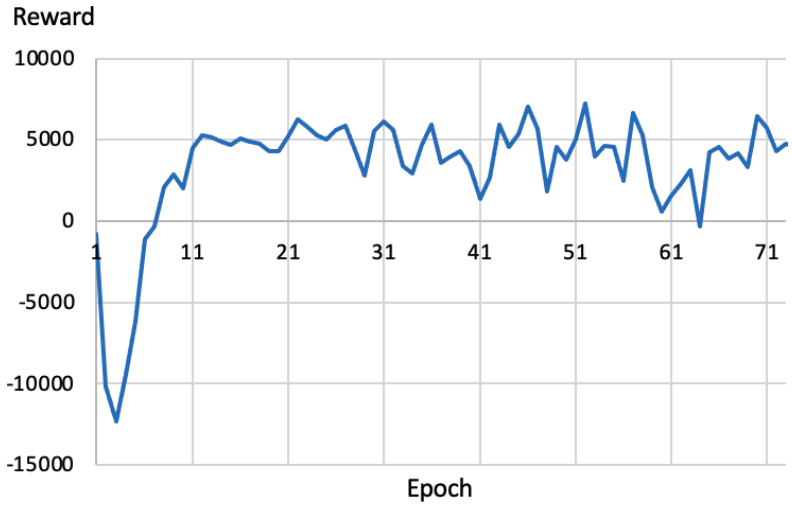

Fig. 30: Cumulative reward v.s. epochs for M = 14 at $ka \in$ [1.35, 1.45]

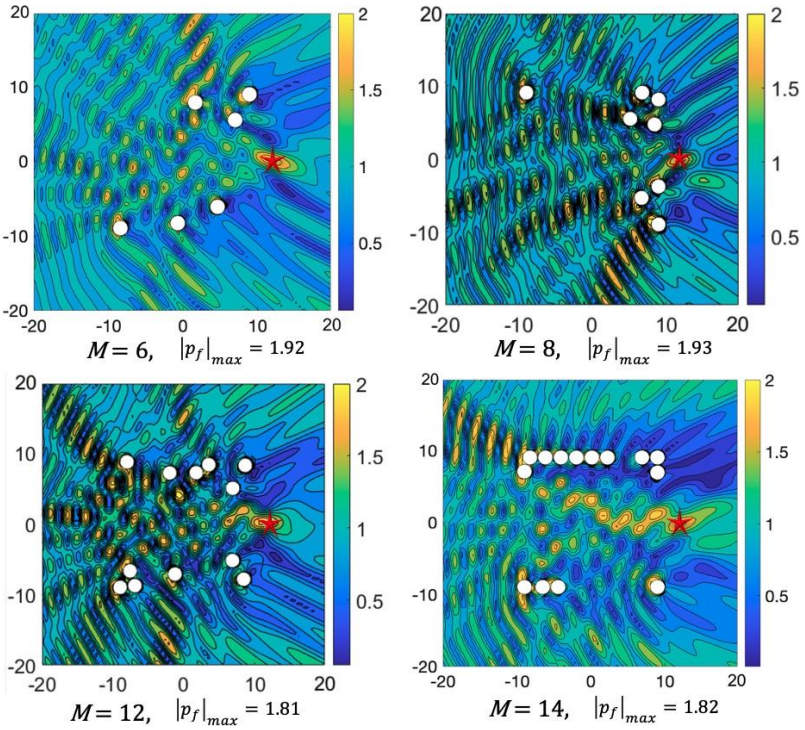

Fig. 31: DDPG results for the total absolute pressure field for M = 6, 8, 12, 14 at ka = 1.40.

clearly noticed at the focal points. Intriguingly, with an increasing number of cylinders, it is ascertained that the cylinders are populated closer and closer to the geometric boundaries.

4.2.3. Dependency of Absolute Pressure Amplitude on ka at a Range of Wavenumbers

4.2.3.1 RL Low Frequency Analysis

RL results are presented and compared to *fmincon* and non-optimized, i.e., random configuration. Fig. 32 shows the pressure amplitude at the focal point at the optimized region for low value of wavenumbers $ka \in [0.35, 0.45]$. The RL model has similar performance compared to *fmincon*.

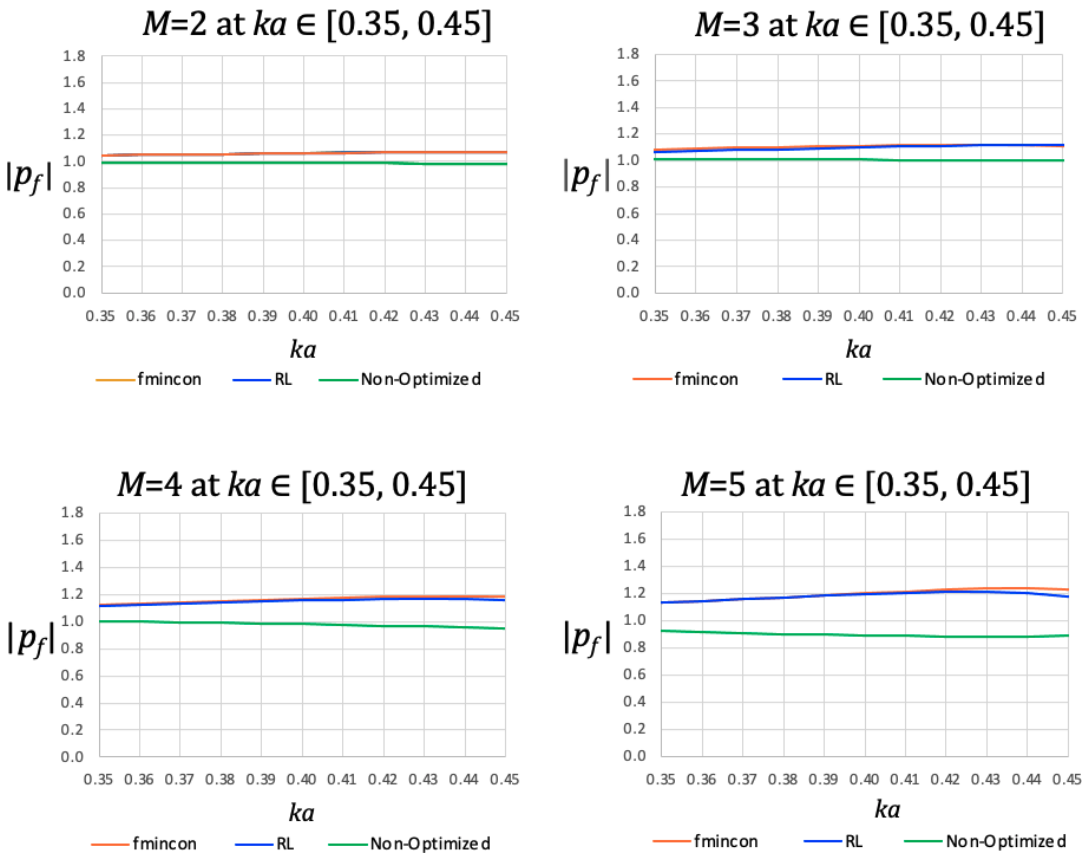

Fig. 32: The dependency of absolute pressure amplitude with normalized wavenumber *ka* at $ka \in [0.35, 0.45]$. Three configurations are considered: *fmincon* (red curve), RL (blue curve), and non-optimized (green curve).

Even though we are focused on the optimized region, i.e., $ka \in [0.35, 0.45]$, Fig. 33 is shown to inspect the performance of the optimized design outside the optimized region. Using the optimized configurations taken from the optimized region, the RL (blue curve), *fmincon* (red curve), and non-optimized (green curve) results have similar performance at $ka \in (0, 0.2]$. For M=2 and M=5 at roughly $ka \in [0.6, 1.0]$, the non-optimized configurations perform better than RL and *fmincon*. Whereas, for $M = 3$ and $M = 4$, RL performs better than *fmincon* and non-optimized results at approximately $ka \in [0.6, 1.0]$.

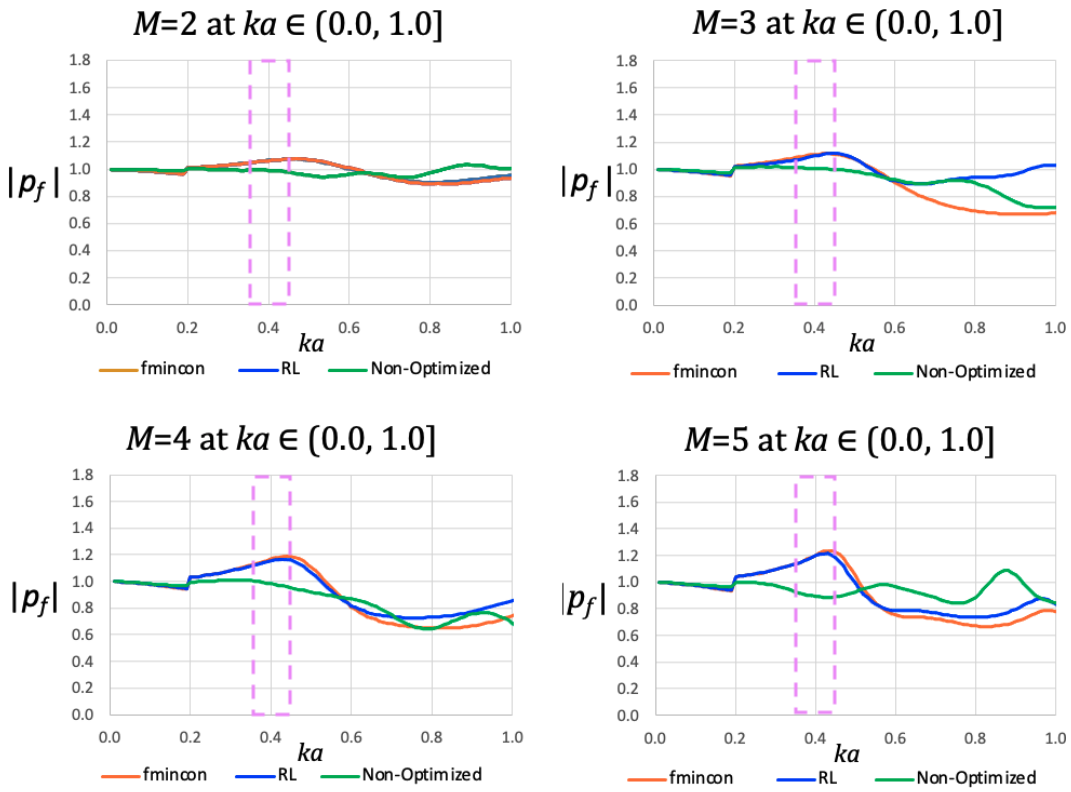

Fig. 33: The dependency of absolute pressure amplitude with normalized wavenumber *ka* at $ka \in (0, 1.0]$, varying the numbers of scatterers $M = 2, 3, 4,$ and $M = 5$. Three configurations are considered: *fmincon* (red curve), RL (blue curve), and non-optimized (green curve). The optimized region, i.e., $ka \in [0.35, 0.45]$ is colored in pink.

4.2.3.2. RL High Frequency Analysis

Fig. 34 presents the variation of absolute pressure amplitude at focal point $|p_f|$ with wavenumber *ka* at *ka* ∈ [1.35, 1.45]. In comparison to *fmincon*, RL model has better performance for *M* = 6 and *M* = 8, but underperforms for *M* = 12. For *M* = 14, RL underperforms *fmincon* solver at *ka* ∈ [1.37, 1.45], but outperforms *fmincon* at *ka* ∈ [1.35, 1.37]. Based on the analysis, the DDPG model has the potential to surpass the performance of *fmincon*.

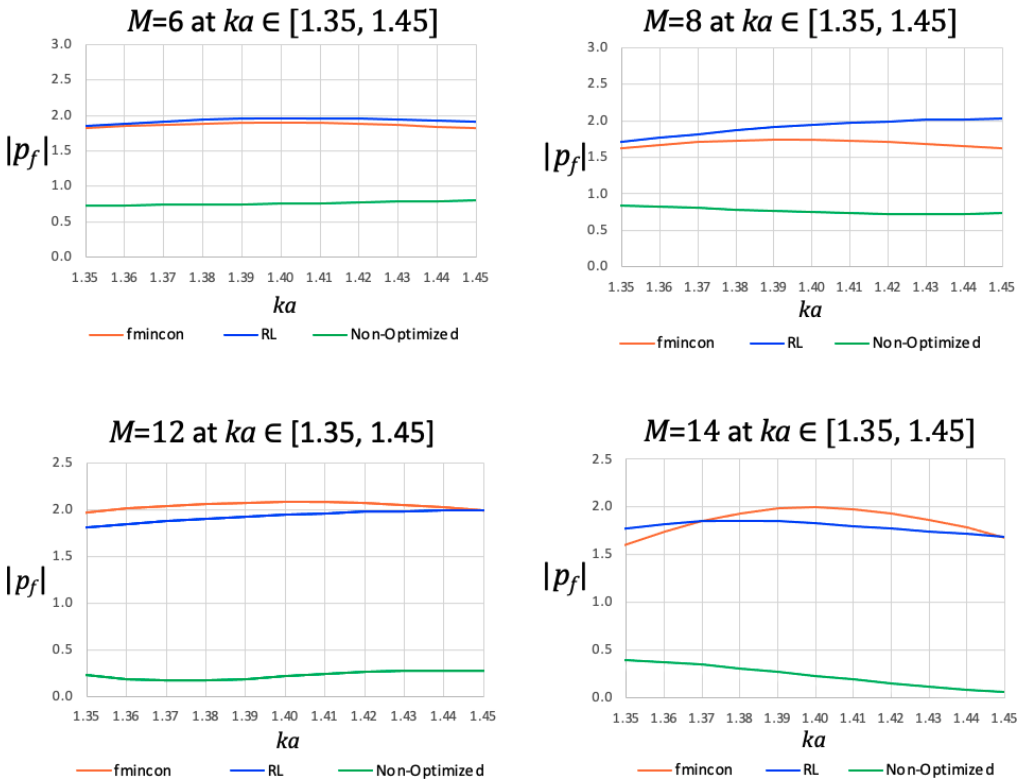

Fig. 34: The dependency of absolute pressure amplitude with normalized wavenumber *ka* ∈ [1.35, 1.45] varying the numbers of scatterers *M* = 6, 8, 12, and *M* = 14.

Fig. 35 shows the absolute pressure amplitude at the focal point $|p_f|$ with wavenumber *ka* at *ka* ∈ (0, 2] using the three configurations, i.e., *fmincon* (red curve), RL (blue curve), and

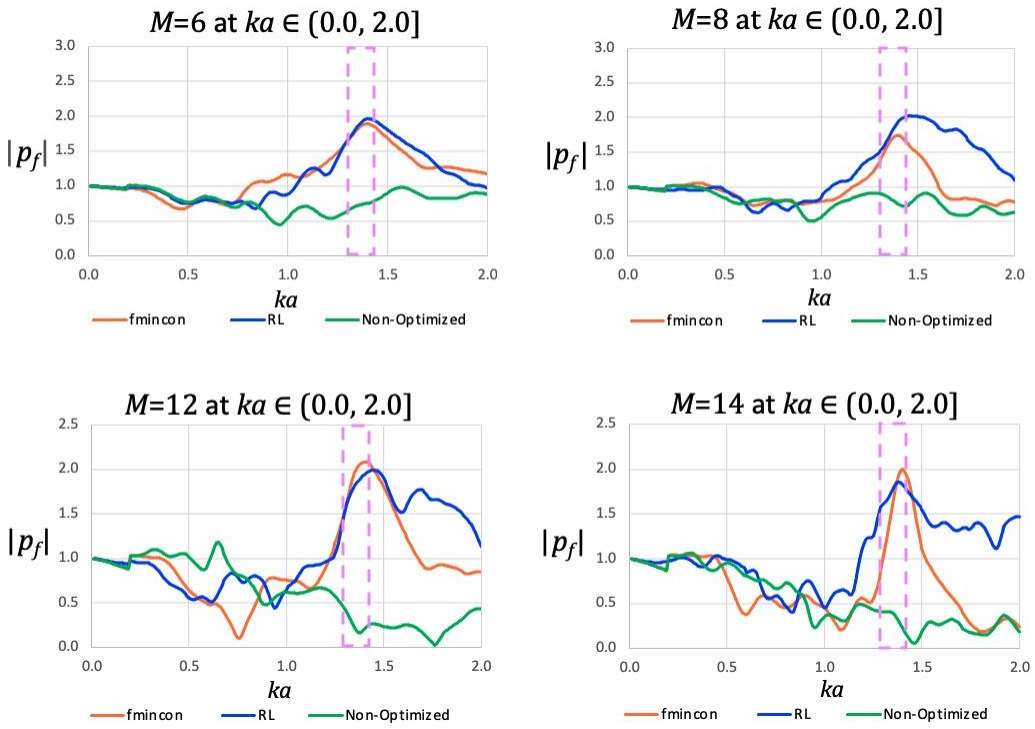

Fig. 35: The optimized region, i.e., $ka \in [1.35, 1.45]$ is colored in pink. The dependency of absolute pressure amplitude with normalized wavenumber at $ka \in (0, 2.0]$ varying the numbers of scatterers $M = 6$, 8, 12, and $M = 14$.

non-optimized (green curve) at the optimized region. For $M = 6$ and $M = 8$ at $ka \in (0, 0.25]$, RL, *fmincon*, and non-optimized have similar performance. The behavior of the three results is a bit complicated roughly at $ka \in [0.5, 1.35]$. As M increases, the complexity of the behavior of RL, *fmincon*, and non-optimized cases increases. Notably, the RL model outperforms *fmincon* even outside the optimized region, especially at a higher value of wavenumbers $ka \in [1.5, 2.0]$ for which the RL model has not been trained.

4.3. Discussion for Reinforcement Learning (RL) Model

We implemented RL model for inverse design of acoustic lens by means if MST. To perform proper comparison, the DDPG model and *fmincon* start from the same initial random configuration. Consequently, the comparison between the DDPG model and *fmincon* is

direct. The RL solution begins to converge when the number of episodes per epoch becomes large. The Julia-based DDPG model makes it possible to run much more episodes per epoch than the Python-Matlab model. The DDPG model may require up to weeks to train, especially when the number of scatterers becomes large. Therefore, it is more difficult for DDPG to achieve convergence rapidly. The important RL results are itemized as follows:

- Due to the complexity of the problem, the reward function plays a critical role. Our current reward function is one of the simplest forms. It might be intriguing to see if a more sophisticated reward function would make the model more effective and require less number of episodes per epoch to obtain converged results.
- At lower frequencies, it is observed that it is difficult to optimize the pressure amplitude because the variation of configurations is low due to having fewer maxima to explore compared to higher frequencies. Unlike the 2D-GLOnets results with a pattern of symmetry at $ka \in [0.35, 0.45]$, as the number of scatterers increases, the optimized configuration becomes more and more asymmetrical, which signifies that it may begin to explore different optima.
- The DDPG model can have more cylinders inside the geometric constraints at higher frequencies. Nevertheless, it is more computationally expensive compared to lower frequencies. With gradient information, the time it takes to converge would reduce [6].

5. CONCLUSION

It has been successfully demonstrated that the 2D-GLOnets and DDPG models can be used to design acoustic lenses. Results show that the 2D-GLOnets generate focusing effects with up to 12 cylinders at $ka \in [0.35, 0.45]$ and $ka \in [1.35, 1.45]$. The optimized absolute pressure amplitude of the 2D-GLOnets converges successfully. Both models' performances are validated by state-of-the-art GBO algorithms of the *fmincon* solver. Increasing the number of scatterers makes it challenging because the reparametrization consumes a great amount of memory for the acoustic lens design problem. With greater computational capabilities, the 2D-GLOnets may produce better the 2D-GLOnets may produce better results than state-of-the-art optimization algorithms.

It is challenging to optimize the design with a lower number of scatterers. In terms of performance, the 2D-GLOnets provide robust optimization results. The lowest values of M for which 2D-GLOnets perform well at $ka \in [0.35, 0.45]$ and $ka \in [1.35, 1.45]$ are 2 and 4, respectively. The lowest value of M for which DDPG performs well at both frequency ranges is 2.

It is computationally expensive to train the DDPG model, but it outperforms the most recent GBO algorithms and provides the means for optimal control of acoustic waves. In addition, DDPG allows more cylinders to be included within the geometric boundaries. Generally, focusing effects become more noticeable at higher wavenumbers, i.e., $ka \in [1.35, 1.45]$. With the current computational resources, DDPG presents good results for $M = 2 \sim 6$ at $ka \in [0.35, 0.45]$. As for $ka \in [1.35, 1.45]$, focusing effects are accomplished. That is to

say; the DDPG model has the potential to account for a much greater number of scatterers with more powerful computing capabilities.

6. FUTURE WORK

- It will be intriguing to look into non-uniform configurations with different design parameters, such as material properties, scatterers' radii, shell structures, etc. Non-uniform configurations of scattering can enhance both DDPG and 2D-GLOnets by varying both radii and positions of the scatterers.
- To speed up the computing time, we can consider using paid high-performance computing, such as AWS, Google Cloud, etc. This will allow more scatterers in the optimized configurations.
- As a result of considering radii variance, the reparametrization scheme would not be necessary, allowing realistic designs with more scatterers in the low-frequency and high-frequency range.
- Furthermore, we will adapt the idea of formulating a generative neural networks-based optimization method utilizing a policy gradient update from Hooten et al. [118].
- Future work will focus on combining the DDPG model with the 2D-GLOnets to improve the performance. There will be additional studies on model-based RL models for the inverse design of acoustic metamaterials, which will be conducted elsewhere.

REFERENCES

[1] J. B. Pendry, D. Schurig, and D. R. Smith, "Controlling electromagnetic fields," *Science*, vol. 312, no. 5781, pp. 1780–1782, 2006.

[2] K. Diest, ed., *Numerical Methods for Metamaterial Design, Topics in Applied Physics*, vol. 127, Springer, 2013.

[3] F. A. Amirkulova, S. Gerges, and A. N. Norris, "Sound localization through multi-scattering and gradient-based optimization," *MDPI Mathematics*, 2021.

[4] F. Amirkulova, L. Zhou, P. Lai, C. Qiu, and T. A. Shah, "Acoustic metamaterial design framework using deep learning and generative modeling," *The Journal of the Acoustical Society of America*, vol. 151, no. A253, 2022.

[5] R. S. Sutton and A. G. Barto, *Reinforcement Learning*. (University of Alberta): MIT Press Ltd, 2018.

[6] T. Shah, L. Zhuo, P. Lai, A. D. L. Rosa-Moreno, F. Amirkulova, and P. Gerstoft, "Reinforcement learning applied to metamaterial design," *Journal of the Acoustical Society of America*, vol. 150, July 2021 https://doi.org/10.1121/10.0005545.

[7] L. Zhuo, "Acoustic cloak design generative modeling and reinforcement learning," Master's thesis, San Jose State University, USA, 2022.

[8] P. Lai, F. Amirkulova, and P. Gerstoft, "Conditional Wasserstein generative adversarial networks applied to acoustic metamaterial design," *The Journal of the Acoustical Society of America*, 2021.

[9] L. Zhuo and F. Amirkulova, "Design of acoustic cloak using generative modeling and gradient-based optimization," in *INTER-NOISE and NOISE-CON Congress and Conference Proceedings*, Institute of Noise Control Engineering, 2021.

[10] N. Wang, W. Yan, Y. Qu, S. Ma, S. Z. Li2, and M. Qiu, "Intelligent designs in nanophotonics: from optimization towards inverse creation," *PhotoniX*, 2021.

[11] Y. Jin, L. He, Z. Wen, H. G. Bohayra Mortazavi, D. Torrent, B. Djafari-Rouhani, T. Rabczuk, X. Zhuang, and Y. Li, "Intelligent on-demand design of phononic metamaterials," *Nanophotonics*, vol. 11, no.3, pp. 439–460, 2022.

[12] I. sajedian, H. Lee, and J. Rho, "Double-deep q-learning to increase the efficiency of metasurface holograms," *Nature*, vol. 9, no. 10899, 2019.

[13] J. Jiang, D. Sell, S. Hoyer, J. Hickey, J. Yang, and J. Fan, "Data-driven metasurface discovery," *arXiv preprint arXiv:1811.12436*, 2019.

[14] P. Packo, A. Norris, and D. Torrent, "Metaclusters for the full control of mechanical waves," *http://arxiv.org/pdf/2009.13376v1*, 2020.

[15] D. Torrent and J. Sánchez-Dehesa, "Radial wave crystals: Radially periodic structures from anisotropic metamaterials for engineering acoustic or electromagnetic waves," *Phys. Rev. Lett.*, vol. 103, no. 6, p. 064301, 2009.

[16] H. Kimizuka, H. Kaburaki, and Y. Kogure, "Mechanism for negative Poisson ratios over the alpha - beta transition of cristobalite, SiO2: A molecular-dynamics study," *Phys. Rev. Lett.*, vol. 84, p. 5548, June 2000.

[17] M. Yang, G. Ma, Z. Yang, and P. Sheng, "Coupled membranes with doubly negative mass density and bulk modulus," *Physical Review Letters*, vol. 110, mar 2013.

[18] H. Chen, S. Zhai, C. Ding, C. Luo, and X. Zhao, "Acoustic metamaterial with negative mass density in water," *J. Appl. Phys.*, vol. 118, p. 094901, sep 2015.

[19] D. J. Colquitt, I. S. Jones, N. V. Movchan, A. B. Movchan, M. Brun, and R. C. McPhedran, "Making waves round a structured cloak: lattices, negative refraction and fringes," *Proceedings of the Royal Society A: Mathematical, Physical and Engineering Sciences*, vol. 469, pp. 20130218–20130218, jul 2013.

[20] A. N. Norris, "Acoustic cloaking theory," *Proc. R. Soc. A*, vol. 464, pp. 2411–2434, 2008.

[21] H. Chen and C. T. Chan, "Acoustic cloaking and transformation acoustics," *J. Phys. D. Appl. Phys.*, vol. 43, no. 11, p. 113001, 2010.

[22] X. Zhou, M. B. Assouar, and M. Oudich, "Acoustic superfocusing by solid phononic crystals," *Appl. Phys. Lett.*, vol. 105, p. 233506, Dec 2014.

[23] B. Choudhury and R. M. Jha, "A review of metamaterial invisibility cloaks," *Tech Science Press*, 2013.

[24] A. Håkansson, F. Cervera, and J. Sánchez-Dehesa, "Sound focusing by flat acoustic lenses without negative refraction," *Appl. Phys. Lett.*, vol. 86, p. 054102, 2005.

[25] A. Spadoni and C. Daraio, "Generation and control of sound bullets with a nonlinear acoustic lens," *Proceedings of the National Academy of Sciences*, vol. 107, pp. 7230–7234, Apr 2010.

[26] H. J. Scholten, Y. Hoever, F. H. van Loon, E. Kanters, T. Hoveling, M. de Wild, R. A. Bouwman, and E. H. Korsten, "Acoustic lens improves superficial in-plane ultrasound-guided procedures – the significance of the beam width artefact," *Journal of Clinical Anesthesia*, 2022.

[27] F. Semperlotti and H. Zhu, "Metamaterial based acoustic lens for structural health monitoring," *United States Patent Application Publication*, 2015.

[28] S. Zhang, L. Yin, and F. N., "Focusing ultrasound with an acoustic metamaterial network," *Physical Review Research*, 2009.

[29] H. Choi, J. J. Jeong, and J. Kim, "Development of an estimation instrument of acoustic lens properties for medical ultrasound transducers," *Journal of Healthcare Engineering*, 2017.

[30] M.-H. Lu, L. Feng, and Y.-F. Chen, "Phononic crystals and acoustic metamaterials," *Materials Today*, vol. 12, pp. 34–42, 12 2009.

[31] X. Lu, X. Wu, H. Xiang, J. Shen, Y. Li, Y. Li, and X. Wang, "Triple tunability of phononic bandgaps for three-dimensional printed hollow sphere lattice metamaterials," *International Journal of Mechanical Sciences*, vol. 221, 03 2022.

[32] A. Li, Z. Luo, H. Wakatsuchi, S. Kim, and D. F. Sievenpiper, "Nonlinear, active, and tunable metasurfaces for advanced electromagnetics applications," *The Journal of the Acoustical Society of America*, 2017.

[33] S. K. Patela, J. Parmara, Y. P. Kostaa, R. Z. Mayurkumar Ladumora, T. K. Nguyend, and V. Dhasarathan, "Design of graphene metasurface based sensitive infrared biosensor," *Sensors and Actuators A: Physical*, vol. 201, 01 2019.

[34] S. K. Patel, S. Charola, J. Parmar, and M. Ladumor, "Broadband metasurface solar absorber in the visible and near-infrared region," *Materials Research Express*, vol. 6, 05 2019.

[35] A. Håkansson, J. Sanchez-Dehesa, and L. Sanchis, "Acoustic lens design by genetic algorithms," *The American Physical Society*, vol. 70, dec 2004.

[36] P. A. Martin, *Multiple Scattering: Interaction of Time-harmonic Waves with N Obstacles*. Cambridge University Press, New York, 2006.

[37] F. D. Reis and N. Karathanasopoulos, "Inverse metamaterial design combining genetic algorithms with asymptotic homogenization schemes," *International Journal of Solids and Structures*, vol. 250, 05 2022.

[38] O. Sigmund, "On the usefulness of non-gradient approaches in topology optimization," *Structural and Multidisciplinary Optimization*, vol. 43, pp. 589–596, mar 2011.

[39] J. Andkjær and O. Sigmund, "Topology optimized low-contrast all-dielectric optical cloak," *Applied Physics Letters*, vol. 98, p. 021112, jan 2011.

[40] Andkjær and O. Sigmund, "Topology optimized acoustic and all-dielectric optical cloaks," *In Photonic Crystals: Moulding the flow of lightroceedings of Metamaterials 2011: The Fifth Inter- national Congress on Advanced Electromagnetic Materials in Microwave and Optics*, vol. 15, 10 2011.

[41] J. Andkjær and O. Sigmund, "Topology optimized cloak for airborne sound," *Journal of Vibration and Acoustics*, vol. 135, p. 041011, 2013.

[42] Y. F. Jingwen Guo, Xin Zhang *, "Topology optimization design and experimental validation of an acoustic metasurface for reflected wavefront modulation," *Journal of Sound and Vibration*, vol. 520, 03 2022.

[43] S. M. Esfarjani, A. Dadashi, and M. Azadi, "Topology optimization of additive-manufactured metamaterial structures: A review focused on multi-material types," *Forces in Mechanics*, vol. 7, 05 2022.

[44] R. Mattosoa, L. Gabrielli, and A. Novotnya, "Topology design optimization of nanophotonic devices for energy concentration," *Applied Mathematical Modelling*, vol. 104, pp. 517–530, 04 2022.

[45] C. Nguyen, X. Zhuang, L. Chamoin, X. Zhao, H. Nguyen-Xuan, and T. Rabczuk, "Three-dimensional topology optimization of auxetic metamaterial using isogeometric analysis and model order reduction," *Computer Methods in Applied Mechanics and Engineering*, vol. 371, 11 2020.

[46] F. A. Amirkulova and A. N. Norris, "The gradient of total multiple scattering cross-section and its application to acoustic cloaking," *Journal of Theoretical and Computational Acoustics*, 2020.

[47] S. G. Feruza A. Amirkulova and A. N. Norris, "Broadband acoustic lens design by reciprocity and optimization," *ASA Express Letters*, vol. 2, no. 024005, 2022.

[48] M. H. Tahersima, K. Kojima, T. Koike-Akino, D. Jha, B. Wang, C. Lin, and K. Parsons, "Deep neural network inverse design of integrated photonic power splitters," *Scientific Reports*, vol. 9, p. 1368, feb 2019.

[49] T. Zhang, J. Wang, Q. Liu, J. Zhou, J. Dai, X. Han, Y. Zhou, and K. Xu, "Efficient spectrum prediction and inverse design for plasmonic waveguide systems based on artificial neural networks," *Photonics Research*, vol. 7, p. 368, mar 2019.

[50] X. Han, Z. Fan, Z. Liu, C. Li, and L. J. Guo, "Inverse design of metasurface optical filters using deep neural network with high degrees of freedom," *InfoMat*, jun 2020.

[51] S. Campbell, D. Sell, E. Jenkins R., Whiting, J. Fan, and D. Werner, "Review of numerical optimization techniques for meta-device design [invited]," *Optical Materials Express*, vol. 9, pp. 1842–1863, Apr. 2019.

[52] Y. Peurifoy, J. Shen, L. Jing, Y. Yang, F. Cano-Renteria, B. DeLacy, J. Joannopoulos, M. Tegmark, and M. Soljac̆ic´, "Nanophotonic particle simulation and inverse design using artificial neural networks," *Sci. Adv.*, vol. 4, no. 6, p. r4206, 2018.

[53] Z. Fan, V. Vineet, H. Gamper, and N. Raghuvanshi, "Fast acoustic scattering using convolutional neural networks," in *ICASSP 2020 - 2020 IEEE International Conference on Acoustics, Speech and Signal Processing (ICASSP)*, IEEE, may 2020.

[54] P. Meng, L. Su, W. Yin, and S. Zhang, "Solving a kind of inverse scattering problem of acoustic waves based on linear sampling method and neural network," *Alexandria Engineering Journal*, vol. 59, pp. 1451–1462, jun 2020.

[55] R. Li, Y. Jiang, R. Zhu, Y. Zou, L. Shen, and B. Zheng, "Design of ultra-thin underwater acoustic metasurface for broadband low-frequency diffuse reflection by deep neural networks," *Nature*, vol. 334, 07 2022.

[56] C. Ma, Y. Chang, S. Wu, and R. R. Zhao, "Deep learning-accelerated designs of tunable magneto-mechanical metamaterials," *American Chemical Society*, 07 2022.

[57] L. Regenwetter, A. H. Nobari, and F. Ahmed, "Deep generative models in engineering design: A review," *ASME*, vol. 144, pp. 1–15, 10 2021.

[58] W. W. Ahmed, M. Farhat, X. Zhang, and Y. Wu, "Deterministic and probabilistic deep learning models for inverse design of broadband acoustic cloak," *Physical Review Research*, vol. 3, 2021.

[59] L. Chen, W. Zhang, Z. Nie, S. Li, and F. Pan, "Generative models for inverse design of inorganic solid materials," *Journal of Materials Informatics*, 07 2021.

[60] J. Ho and S. Ermon, "Generative adversarial imitation learning," *arXiv*, 06 2016.

[61] I. J. Goodfellow, J. Pouget-Abadie, M. Mirza, B. Xu, D. Warde-Farley, S. Ozair, A. Courville, and Y. Bengio, "Generative adversarial nets," in *Advances in Neural Information Processing Systems 27 (NIPS 2014)*, 2014.

[62] M. Kingma, D. Welling, "Auto-encoding variational bayes," *arXiv:1312.6114v10*, 2014.

[63] M. Mirza and S. Osindero, "Conditional Generative Adversarial Nets," *arXiv:1411.1784v1*, 2014.

[64] M. Arjovsky, S. Chintala, and L. Bottou, "Wasserstein Generative Adversarial Networks," in *Proceedings of the 34th International Conference on Machine Learning*, 2017.

[65] Y. Boget, "Adversarial regression. Generative adversarial networks for non-linear regression: Theory and assessment," Master's thesis, University of Neuchâtel, 2019.

[66] K. T. Butler, D. W. Davies, H. Cartwright, O. Isayev, and A. Walsh, "Machine learning for molecular and materials science," *Nature*, vol. 559, pp. 547–555, jul 2018.

[67] A.-P. Blanchard-Dionne and O. J. F. Martin, "Successive training of a generative adversarial network for the design of an optical cloak," *OSA Continuum*, vol. 4, p. 87, dec 2020.

[68] J. Jiang, D. Sell, S. Hoyer, J. Hickey, J. Yang, and J. A. Fan, "Free-form diffractive metagrating design based on generative adversarial networks," *ACS Nano*, vol. 13, pp. 8872–8878, jul 2019.

[69] C. Gurbuz, F. Kronowetter, C. Dietz, M. Eser, J. Schmid, and S. Marburg, "Generative adversarial networks for the design of acoustic metamaterials," *The Journal of the Acoustical Society of America*, vol. 149, pp. 1162–1174, feb 2021.

[70] L. H, L. X., W. X., and W. Y., "On a novel inverse scattering scheme using resonant modes with enhanced imaging resolution.," *arXiv:1805.10473*, 2018.

[71] J. Jiang and J. A. Fan, "Global optimization of dielectric metasurfaces using a physics-driven neural network," *Nano Letters*, vol. 19, pp. 5366–5372, jul 2019.

[72] J. Rho and J. A. Fan, "Freeform metasurface design based on topology optimization," *MRS Bulletin*, vol. 45, no. 3, pp. 196–201, 2020.

[73] M. Chen, J. Jiang, and J. Fan, "Design space reparameterization enforces hard geometric constraints in inverse-designed nanophotonic devices," *ACS Photonics*, vol. 11, 2020.

[74] T. Blaschke, M. Olivecrona, O. Engkvist, J. Bajorath, and H. Chen, "Application of generative autoencoder in de novo molecular design," *arXiv*, 11 2017.

[75] J. Wang, Y. Wang, and Y. Chen, "Inverse design of materials by machine learning," *MDPI*, vol. 15, 02 2022.

[76] L. Wang, Y.-C. Chan, F. Ahmed, Z. Liu, P. Zhu, and W. Chen, "Deep generative modeling for mechanistic-based learning and design of metamaterial systems," *arXiv*, 09 2020.

[77] T. Tran, F. Amirkulova, and E. Khatami, “Acoustic cloak design via machine learning,” *Journal of Theoretical and Computational Acoustics*, vol. (accepted), 07 2022.

[78] T. Tran, E. Khatami, and F. Amirkulova, “Total multiple scattering cross section evaluation using convolutional neural networks for forward and inverse designs of acoustic metamaterials,” *Journal of the Acoustical Society of America*, vol. 149, 06 2021.

[79] F. Amirkulova, T. Tran, and E. Khatami, “Generative deep learning model for broadband acoustic metamaterial design,” *Journal of the Acoustical Society of America*, vol. 150, 11 2021.

[80] W. W. Ahmed, M. Farhat, P.-Y. Chen, X. Zhang, and Y. Wu, “A generative deep learning approach for shape recognition of arbitrary objects from phaseless acoustic scattering data,” *arXiv*, 07 2022.

[81] S. Gupta, G. Singal, and D. Garg, “Deep reinforcement learning techniques in diversified domains: A survey,” *Archives of Computational Methods in Engineering*, vol. 28, 02 2021.

[82] R. S. Sutton and A. G. Barto, *Reinforcement Learning: An Introduction*. The MIT Press Cambridge, Massachusetts, 2014.

[83] G. L. Guimaraes, B. Sanchez-Lengeling, C. Outeiral, P. L. C. Farias, and A. Aspuru-Guzik, “Objective-reinforced generative adversarial networks (ORGAN) for sequence generation models,” *arXiv:1705.10843v3*, 2017.

[84] E. Putin, A. Asadulaev, Y. Ivanenkov, V. Aladinskiy, B. Sanchez-Lengeling, A. Aspuru-Guzik, and A. Zhavoronkov, “Reinforced adversarial neural computer for de novo molecular design,” *Journal of Chemical Information and Modeling*, vol. 58, pp. 1194–1204, may 2018.

[85] M. Popova, O. Isayev, and A. Tropsha, “Deep reinforcement learning for de novo drug design,” *Science Advances*, vol. 4, 07 2018.

[86] Z. Zhou, S. Kearnes, L. Li, R. N. Zare, and P. Riley, “Optimization of molecules via deep reinforcement learning,” *Scientific Reports*, vol. 9, 07 2019.

[87] W. Hu, “Reinforcement learning of molecule optimization with bayesian neural networks,” *Computational Molecular Bioscience*, vol. 11, p. 69–83, 2021.

[88] W. Hu, “Exploring local chemical space in de novo molecular generation using multi-agent deep reinforcement learning,” *Natural Science*, vol. 13, p. 412–424, 2021.

[89] W. Hu, “Inverse molecule design with invertible neural networks as generative models,” *Journal of Biomedical Science and Engineering*, vol. 14, p. 305–315, 2021.

[90] I. Sajedian, H. Lee, and J. Rho, “Double-deep q-learning to increase the efficiency of metasurface holograms,” *Scientific Reports*, vol. 9, jul 2019.

[91] I. Sajedian, T. Badloe, H. Lee, and J. Rho, “Deep q-network to produce polarization-independent perfect solar absorbers: a statistical report,” *Nano Convergence*, vol. 7, aug 2020.

[92] T. Badloe, I. Kim, and J. Rho, “Biomimetic ultra-broadband perfect absorbers optimised with reinforcement learning,” *Physical Chemistry Chemical Physics*, vol. 22, no. 4, pp. 2337–2342, 2020.

[93] S. So, T. Badloe, J. Noh, J. Rho, and J. Bravo-Abad, “Deep learning enabled inverse design in nanophotonics,” *Nanophotonics*, vol. 9, pp. 1041–1057, feb 2020.

[94] B. Sanchez-Lengeling and A. Aspuru-Guzik, “Inverse molecular design using machine learning: Generative models for matter engineering,” *Science*, vol. 361, pp. 360–365, jul 2018.

[95] D. Silver, T. Hubert, J. Schrittwieser, I. Antonoglou, M. Lai, A. Guez, M. Lanctot, L. Sifre, D. Kumaran, T. Graepel, T. Lillicrap, K. Simonyan, and D. Hassabis, “A general reinforcement learning algorithm that masters chess, shogi, and Go through self-play,” *Science*, Jan 2019.

[96] T. P. Lillicrap, J. J. Hunt, A. Pritzel, N. Heess, T. Erez, Y. Tassa, D. Silver, and D. Wierstra, “Continuous control with deep reinforcement learning,” *https://arxiv.org/abs/1509.02971*, 2015.

[97] Y. Hou, L. Liu, Q. W. X. Xua, and C. Chen, “A novel ddpg method with prioritized experience replay,” *2017 IEEE International Conference on Systems, Man, and Cybernetics (SMC)*, 2017.

[98] E. Anderlini, G. G. Parker, and G. Thomas, “Docking control of an autonomous underwater vehicle using reinforcement learning,” *MDPI*, vol. 9, no. 3456, 2019.

[99] S. K. Kim, P. P. Li, J. T. Kim, P. Karande, and Y.-J. T. Han, “Optimizing 3d structure of h2o molecule using ddpg,” *Proceedings of the 36th International Conference on Machine Learning*, 2019.

[100] J. Tordesillas and J. Arbelaiz, “Personalized cancer chemotherapy schedule: a numerical comparison of performance and robustness in model-based and model-free scheduling methodologies,” *arXiv*, 2019.

[101] F. A. Amirkulova, *Acoustic and Elastic Multiple Scattering and Radiation from Cylindrical Structures*. PhD thesis, Rutgers University, Piscataway, NJ, USA, 2014.

[102] F. Amirkulova and A. N. Norris, "Acoustic multiple scattering using fast iterative techniques," in *ASME IMECE Conference. Tampa, FL.*, pp. IMECE2017–72249, 2017.

[103] K. Gurney, *An introduction to neural networks*. University of Sheffield, 2004.

[104] M. A. Nielsen, *Neural Networks and Deep Learning*. Determination Press, 2015.

[105] I. Goodfellow, Y. Bengio, and A. Courville, *Deep Learning*. MIT Press, 2016.

[106] D. R. L. Pornaras, W.-C. Wang, Y. Chen, G. Kwak, F. Amirkulova, and E. Khatami, "Broadband suppression of total multiple scattering cross section using neural networks," *The Journal of the Acoustical Society of America*, vol. 146, pp. 2876–2877, oct 2019.

[107] W. C. Wang, D. R. Pornaras, R. Gonzales, and F. Amirkulova, "Broadband suppression of total multiple scattering cross section using neural networks.," in *Proceeding of Asian Pacific Congress on Computational Mechanics (APCOM)*, 2019.

[108] W.-C. Wang, "Sound localization via deep learning, generative modeling, and global optimization," *The Journal of the Acoustical Society of America*, vol. 151, 05 2022.

[109] W.-C. Wang, F. Amirkulova, and L. Zhuo, "The 2d-global optimization networks (2d-glonets) model for acoustic metamaterial design," *International Congress on Acoustics*, 05 2022.

[110] W.-C. Wang, "Generative modeling and reinforcement learning for acoustic lens design," *International Society for Optics and Photonics*, 08 2022.

[111] T. M. Inc, "Train multiple agents to perform collaborative task," may 2021. https://www.mathworks.com/help/reinforcement-learning/ug/train-2-agents-to-collaborate.html.

[112] H. van Hasselt, A. Guez, and D. Silver, "Deep reinforcement learning with double Q-learning," *https://arxiv.org/abs/1509.06461*, 2015.

[113] Z. Fu, D. Zhan, X. Li, and Y. Lu, "Automatic successive reinforcement learning with multiple auxiliary rewards," in *Twenty-Eighth International Joint Conference on Artificial Intelligence*, 2019.

[114] O. S. Guillaume Matheron, Nicolas Perrin, "The problem with ddpg: understanding failures in deterministic environments with sparse rewards," *International Conference on Learning Representations*, 2019.

[115] W.-C. Wang, “Amirkulovalab,” Aug 2022. https://github.com/AmirkulovaLab/RL_Julia.jl

[116] Y. Liu, Z. Jiang, S. Zhang, and S. Xu, “Deep reinforcement learning-based beam tracking for low-latency services in vehicular networks,” *Institute of Electrical and Electronics Engineers*, 2020.

[117] T. Kobayashi and W. E. L. Ilboudo, “T-soft update of target network for deep reinforcement learning,” *Nara Institute of Science and Technology*, 2020.

[118] S. Hooten, R. G. Beausoleil, S. K. Vadlamani, and T. V. Vaerenbergh, “Generative neural network based non-convex optimization using policy gradients with an application to electromagnetic design,” *NeurIPS*, 2021.